CMS Physics Analysis Summary

Contact: cms-pag-conveners-susy@cern.ch 2022/03/28

Search for supersymmetry in final states with a single electron or muon using angular correlations and heavy object tagging in proton-proton collisions at $\sqrt{s} = 13$ TeV

The CMS Collaboration

Abstract

A search for supersymmetry is presented in events with a single charged lepton (electron or muon) and multiple hadronic jets. The data correspond to a sample of proton-proton collisions at $\sqrt{s} = 13$ TeV with an integrated luminosity of 138 fb^{-1}, recorded by the CMS experiment at the LHC. The search targets gluino pair production, where the gluinos decay into the lightest supersymmetric particle (LSP) and either a top quark-antiquark pair, or a light-flavor quark-antiquark pair and a W boson. Depending on the targeted scenario, some of the jets are required to be identified as originating from b quarks. The main backgrounds, top quark pair production and W+jets production, are suppressed by requirements on the azimuthal angle between the lepton momentum and the reconstructed leptonic W boson candidate, and by top quark and W boson tagging based on a machine-learning technique. A number of exclusive search regions are defined according to the number of jets and several kinematic variables. The number of observed events is consistent with the expectations from standard model processes, and the results are used to set limits on supersymmetric particle masses in the context of two simplified models of gluino pair production. Exclusions for gluino masses reach up to 2130 (2280) GeV at 95% confidence level for a model with gluino decay to a top quark-antiquark pair (a light-flavor quark-antiquark pair and a W boson) and the LSP. For the same models, limits on the mass of the LSP reach up to 1270 (1220) GeV.

1 Introduction

Supersymmetry (SUSY) [1–6] is a well-known extension of the standard model (SM) of particle physics, which is able to address several shortcomings of the SM by introducing a new symmetry that predicts additional superpartners to the existing bosons and fermions. The supersymmetric partner particle of the gluon is the gluino ($\widetilde{\mathrm{g}}$). The superpartners of the electroweak gauge bosons and the Higgs bosons mix to form mass eigenstates called neutralinos ($\widetilde{\chi}^0$) and charginos ($\widetilde{\chi}^{\pm}$). In SUSY models that conserve *R*-parity [7], the SUSY particles have to be produced in pairs and the lightest SUSY particle (LSP) is stable, providing a viable dark matter candidate.

The search presented in this document targets final states containing a single lepton (electron or muon), missing transverse momentum, and large hadronic activity, using 138 fb^{-1} of proton-proton collisions at 13 TeV data recorded with the CMS experiment at the CERN LHC during Run 2 (2016–2018). By defining exclusive search regions with and without b-tagging requirements, the search is sensitive to different SUSY models. The sensitivity is further enhanced by a large number of search region bins defined by several variables. The results are interpreted in terms of simplified models [8–12].

The diagrams of the specific *R*-parity conserving models of gluino pair production that are used to interpret the results are shown in Fig. 1. The results of the search with at least one b-tagged jet, referred to as multi-b analysis, are interpreted in terms of the simplified model T1tttt (left), where the gluino always decays to a top quark-antiquark pair ($\mathrm{t\bar{t}}$) and the lightest neutralino ($\widetilde{\chi}^0_1$), which is the LSP. The observations in the search region bins with no b-tagged jets, referred to as zero-b analysis, are interpreted in the model T5qqqqWW (right). In this model, each gluino decays to a (light flavor) quark-antiquark pair ($\mathrm{q\bar{q}'}$) and the lighter chargino ($\widetilde{\chi}^{\pm}_1$), which then decays further to a W boson and the $\widetilde{\chi}^0_1$. The mass of the $\widetilde{\chi}^{\pm}_1$ is fixed at the value halfway between the masses of the $\widetilde{\mathrm{g}}$ and the $\widetilde{\chi}^0_1$.

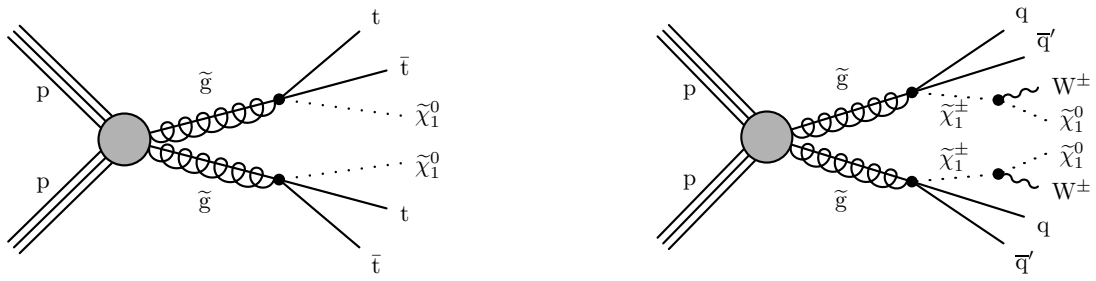

Figure 1: Diagrams showing the simplified SUSY models (left) T1tttt and (right) T5qqqqWW. In T5qqqqWW, the W boson can be virtual depending on the mass difference between the chargino ($\widetilde{\chi}^{\pm}$) and the neutralino ($\widetilde{\chi}^0_1$).

Searches targeting gluino production in the single-lepton final state have been performed both by the ATLAS [13–17] and CMS [18–23] Collaborations. The investigated models have also been tested by ATLAS [24–27] and CMS [28–35] in other final states.

The results presented in this paper improve with respect to the CMS search presented in Ref. [19], which follows a similar strategy and uses 35.9 fb^{-1} of data recorded in 2016, not only because of the larger analyzed data set, but also by significantly reducing the background contributions in the search region. This is achieved by the requirement of one or more jets to be consistent with a hadronically decaying top quark (W boson) in the multi-b (zero-b) final states as determined by multivariate classifiers.

2 The CMS detector

The CMS detector is a general-purpose particle detector surrounding the luminous region where protons from the LHC beams interact. A 3.8 T magnetic field is produced by a solenoid of 6 m internal diameter, within which are a silicon pixel and silicon strip tracking detector, a lead tungstate crystal electromagnetic calorimeter (ECAL), and a brass and scintillator hadronic calorimeter (HCAL). Each of these parts of the detector is composed of a cylindrical barrel section and two endcap sections. The pseudorapidity (η) coverage of the barrel and endcap detectors is extended by forward calorimeters that lie very close to the LHC beam line. Outside the solenoid, returning magnetic flux is guided through a steel return yoke. Gas-ionization detectors are sandwiched in between the layers of the return yoke and are used to detect muons. The events used in the search were collected in 2016–2018 using a two-tiered trigger system: The first level (L1), composed of custom hardware processors, uses information from the calorimeters and muon detectors to select events at a rate of around 100 kHz within a fixed latency of about 4 μs [36]. The second level, known as the high-level trigger (HLT), consists of a farm of processors running a version of the full event reconstruction software optimized for fast processing, and reduces the event rate to around 1 kHz before data storage [37]. The CMS detector is described in more detail, along with the coordinate system and basic kinematic variables, in Ref. [38].

3 Simulation

Simulated background events are used to optimize the event selection and test the background estimation, which is mainly based on control samples in data. The SM processes are simulated with different Monte Carlo (MC) event generators: Events for $\mathrm{t\bar{t}}$, W+jets, and Drell–Yan (DY) production, as well as for the background from SM events composed uniquely of jets produced through the strong interaction, referred to as quantum chromodynamics (QCD) multijet events, are simulated using the MADGRAPH5_aMC@NLO event generator at leading order (LO) (versions 2.2.2 for 2016 and 2.4.2 for 2017 and 2018) [39]. The $\mathrm{t\bar{t}}$ events are generated with up to three additional partons in the matrix-element calculation, while the W+jets and DY events are generated with up to four additional partons. Single top quark events produced through the s channel, events containing a $\mathrm{t\bar{t}}$ pair produced in association with a Z boson, a W boson, or a photon, and rare events such as those containing multiple electroweak or Higgs bosons (W, Z, γ, and H) are generated with MADGRAPH5_aMC@NLO at next-to-LO (NLO) [40]. Events containing a single top quark produced through the t channel and tW production, as well as WW and $\mathrm{t\bar{t}H}$ events, are simulated with the POWHEG v1 (v2) [41–48] program at NLO for 2016 (2017 and 2018). The ZZ events are generated at NLO with either POWHEG or MADGRAPH5_aMC@NLO depending on the decay mode, while WZ production is simulated with PYTHIA 8.226 (8.230) [49] for 2016 (2017 and 2018) at LO. The normalization of the simulated background samples is performed using the most accurate cross section calculations available [39, 44, 45, 50–61], which typically correspond to NLO or next-to-NLO (NNLO) accuracy.

Simulated signal events are generated using MADGRAPH5_aMC@NLO at LO including up to two additional partons in the matrix-element calculation. The production cross sections are determined with approximate NNLO plus next-to-next-to-leading logarithmic (NNLL) corrections [62–72]. The signal events are produced on a two-dimensional grid for different gluino and LSP masses.

The parton showering and hadronization for all simulated samples is performed with the

PYTHIA 8.226 (8.230) program for 2016 (2017 and 2018). Samples that are simulated at NLO with MADGRAPH5_aMC@NLO match partons from the matrix-element calculation to those from parton showers using the FxFx [40] scheme, while for samples simulated at LO the MLM scheme [73] is adopted. The CUETP8M1 [74] PYTHIA 8.226 tune is used for both SM and signal samples for the analysis of the 2016 data. For 2017 and 2018, the CP5 (CP2) [75] tunes are used for the SM background (signal) samples. Simulated samples generated at LO or NLO with the CUETP8M1 tune use the NNPDF2.3LO or NNPDF2.3NLO [76] parton distribution functions (PDFs), respectively. The samples using the CP2 or CP5 tune use the NNPDF3.1LO or NNPDF3.1NNLO [77] PDFs, respectively.

Simulated SM events are processed through a GEANT4-based [78] simulation of the CMS detector, while the simulated signal events are processed through the CMS fast simulation program [79, 80] in order to save computational processing time. The results of the fast simulation are found to be generally consistent with the GEANT4-based simulation.

All simulated events are generated with nominal distributions of additional pp interactions per bunch crossing, referred to as pileup. The simulation is reweighted to match the corresponding pileup distribution measured in data.

In order to improve the modeling of additional jets originating mainly from initial-state radiation (ISR) in events containing $\mathrm{t\bar{t}}$, the MADGRAPH5_aMC@NLO prediction is compared to data in a $\mathrm{t\bar{t}}$-enriched dileptonic control region, and scale factors are extracted that are applied to the 2016 $\mathrm{t\bar{t}}$ simulation as well as on the SUSY signal simulation. The $\mathrm{t\bar{t}}$ simulation of the years 2017 and 2018 is done with an updated tune resulting in a good agreement between simulation and data, such that no scale factors are needed.

4 Object reconstruction

The particle-flow (PF) algorithm [81] aims to reconstruct and identify each particle in an event, with an optimized combination of information from the various elements of the CMS detector, and identifies each as a photon, electron, muon, charged hadron, or neutral hadron. The energy of charged hadrons is determined from a combination of their momentum measured in the tracker and the matching ECAL and HCAL energy deposits, corrected for the response function of the calorimeters to hadronic showers. The energy of neutral hadrons is obtained from the corresponding corrected ECAL and HCAL energies. The primary vertex (PV) is taken to be the vertex corresponding to the hardest scattering in the event, evaluated using tracking information alone, as described in Section 9.4.1 of Ref. [82].

The energy of electrons is determined from a combination of the electron momentum at the PV as determined by the tracker, the energy of the corresponding ECAL cluster, and the energy sum of all bremsstrahlung photons spatially compatible with originating from the electron track [83]. The electron momentum is estimated by combining the energy measurement in the ECAL with the momentum measurement in the tracker. For electrons with transverse momentum $p_{\mathrm{T}} \approx 45\,\mathrm{GeV}$ from $\mathrm{Z} \to \mathrm{e^+e^-}$ decays, the momentum resolution ranges from 1.7 to 4.5%. It is generally better in the barrel region than in the endcaps, and also depends on the bremsstrahlung energy emitted by the electron as it traverses the material in front of the ECAL.

The energy of muons is obtained from the curvature of the corresponding track. Muons are measured in the pseudorapidity range $|\eta| < 2.4$, with detection planes made using three technologies: drift tubes, cathode strip chambers, and resistive plate chambers. Matching muons to tracks measured in the silicon tracker results in a relative transverse momentum resolution,

for muons with p_T up to 100 GeV, of 1% in the barrel and 3% in the endcaps. The p_T resolution in the barrel is better than 7% for muons with p_T up to 1 TeV [84].

Two categories of light leptons are defined, denoted by "veto leptons" and "good leptons", with a minimum p_T threshold of 10 and 25 GeV, respectively. Muons that fulfill the "loose" working point (WP) of the standard muon identification (ID) criteria [84] are defined as "veto muons". The efficiency for reconstructing a "veto muon" exceeds 99%. The dedicated "veto" WP of the standard electron ID criteria [83] is used to define "veto electrons", which corresponds to an efficiency of 95%. The "medium" WP of the muon ID criteria with an efficiency of more than 98% is used to select good muons. Good electrons are selected using the "tight" WP of the electron ID criteria with an efficiency of 70%. A conversion veto and the requirement of zero lost hits in the inner tracker are applied for good electrons to reject converted photons.

A relative isolation variable is defined as the p_T sum of all objects within a cone around the lepton candidate (excluding the candidate itself), divided by the lepton p_T. This variable describes the activity around the lepton. This analysis uses the so-called mini-isolation variable (I_{mini}), where the cone size R, referring to the distance in the ϕ–η plane, depends on the p_T of the lepton: for $p_T < 50$ GeV, $R = 0.2$; for $50 < p_T < 200$ GeV, $R = 10\text{GeV}/p_T$; and for $p_T > 200$ GeV, $R = 0.05$. We use a common requirement of $I_{mini} < 0.4$ for all veto leptons, whereas for good muons (electrons) $I_{mini} < 0.2$ (0.1) is required. The use of I_{mini} enhances the selection efficiency of signal events that contain a large amount of hadronic energy.

Jets are clustered with the anti-k_T algorithm [85, 86] with a distance parameter R of 0.4, or, in order to identify large-radius jets, with $R = 0.8$. The jet momentum is determined as the vectorial sum of all particle momenta in the jet, and is found from simulation to be, on average, within 5 to 10% of the true momentum over the whole p_T spectrum and detector acceptance. Additional proton-proton interactions within the same or nearby bunch crossings can contribute additional tracks and calorimetric energy depositions, increasing the apparent jet momentum. To mitigate this effect, tracks identified to be originating from pileup vertices are discarded and an offset correction is applied to correct for remaining contributions [87]. Jet energy corrections are derived from simulation studies so that the average measured energy of jets becomes identical to that of particle level jets. In situ measurements of the momentum balance in dijet, photon+jet, Z+jet, and multijet events are used to determine any residual differences between the jet energy scale in data and in simulation, and appropriate corrections are made [88]. Additional selection criteria are applied to each jet to remove jets potentially affected by instrumental effects or reconstruction failures. Jets are selected with $p_T > 30$ GeV and $|\eta| < 2.4$. For the fast simulation that is used for the signal, dedicated jet energy corrections are applied. Jets that lie within a cone of $R = 0.4$ around any good or veto lepton are removed, to avoid double counting.

To identify jets originating from b quarks, an inclusive deep neural network based Combined Secondary Vertex tagger is used with a medium working point [89]. The efficiency to identify b jets varies between 50 and 70%, depending on the jet p_T, with a misidentification probability of 10–15% for c jets and 1–5% for light flavor and gluon jets, also depending on the jet p_T.

In order to identify hadronic decays of top quarks and W bosons with a large Lorentz boost we apply a special tagging algorithm that is based on machine learning, the so-called DeepAK8 algorithm [90]. It acts on jets with the distance parameter of $R = 0.8$ (AK8 jets) and is a multiclass classifier for top quark, W boson, Z boson, Higgs boson, and QCD jets. It builds upon a deep neural network taking input from all the PF candidates and secondary vertices that comprise the AK8 jet.

Hadronically decaying top quarks with $p_T > 400\,\text{GeV}$ are usually merged into one large-radius jet, and are identified using the DeepAK8 algorithm with a "loose" working point, with an efficiency of ≈68% with a mistagging rate of ≈8%. Top quarks with $p_T < 400\,\text{GeV}$ are usually not boosted enough to be caught in one large-radius jet cone, and therefore identified by a resolved top quark tagging algorithm, first used in Ref. [91]. It identifies hadronically decaying top quarks whose decay products are forming three individual jets with the standard radius of $R = 0.4$. A boosted decision tree is used to distinguish between trijet combinations whose three jets all match the decay products of a top quark versus those that do not. It uses high-level information such as the invariant mass of the trijet as well as information from each jet. The resolved top quark tagger yields an efficiency of ≈42%, while the mistagging rate is ≈4%.

To avoid double counting, a cross cleaning between resolved and merged top quark tags is performed by first reconstructing the merged top quarks as identified by the DeepAK8 algorithm. In the next step, resolved top quark candidates that contain any jet within a cone of a radius $R = 0.8$ of the merged top quark (i.e., the cone within which the DeepAK8 algorithm searches for top quarks) are removed. In the following, n_t is used to denote the number of identified top quark jets (top tags).

Hadronically decaying W bosons are identified with the DeepAK8 algorithm as well. For the zero-b channel, this tagging algorithm utilizes AK8 jets to identify hadronically decaying W bosons with $p_T > 200\,\text{GeV}$ using the "tight" working point. The efficiency for W boson tagging is ≈62%, while the mistagging rate is ≈7%. The number of identified W bosons is given by n_W.

The missing transverse momentum vector $\vec{p}_T^{\,\text{miss}}$ is computed as the negative vector sum of the transverse momenta of all the PF candidates in an event, and its magnitude is denoted as p_T^{miss} [92]. The $\vec{p}_T^{\,\text{miss}}$ is modified to account for corrections to the energy scale of the reconstructed jets in the event. Anomalous high-p_T^{miss} events can occur because of a variety of reconstruction failures, detector malfunctions or non-collision backgrounds. Such events are rejected by event filters that are designed to identify more than 85–90% of the spurious high-p_T^{miss} events with a mistagging rate of less than 0.1%.

Two kinematic variables are used to describe the energy scale of an event: The L_T variable is defined as the scalar sum of the lepton p_T and the missing transverse momentum p_T^{miss}, reflecting the "leptonic" energy scale of the event. The H_T variable reflects the "hadronic" energy scale of the event. It is referred to the scalar sum of the p_T of all selected jets.

In the second half of the 2018 data-taking period, a detector malfunction prevented the readout from 3% of the hadron calorimeter. This is taken into account by reweighting simulated events such as to reflect the overall 2018 efficiency of the hadron calorimeter in the relevant region.

5 Baseline event selection

Events are selected with a combination of different HLT paths, relying on reconstructed leptons, H_T, p_T^{miss}, or combinations thereof, to maximize the trigger efficiency. The main HLT path requires a loosely isolated electron or muon with $p_T > 15\,\text{GeV}$ and $H_T > 350$, 400, and 450 GeV for 2016, 2017, and 2018, respectively. The additional HLT paths require $p_T^{\text{miss}} > 100$, 110, and 120 GeV for the three data-taking years; isolated electrons with $p_T > 27$ (35) GeV in 2016 (2017 and 2018); isolated muons with $p_T > 24\,\text{GeV}$; or leptons with no isolation requirement and a higher p_T threshold of 105 or 115 GeV for electrons (depending on the year), or 50 GeV for muons. The trigger efficiency is measured in control samples recorded either with single-lepton triggers or with triggers based on an H_T requirement. For the electron channel, it is found to

be 98, 93, and 97% in 2016, 2017, and 2018, respectively, while for the muon channel it is 99% for all three years. The inefficiency is mainly caused by the lepton selection in the trigger. The uncertainty in the measured trigger efficiencies is about 1%.

For the baseline event selection, one good electron or muon (called lepton in the following) with $p_T > 25\,\text{GeV}$ is required, and events with additional veto leptons with $p_T > 10\,\text{GeV}$ are removed. Events with two genuine leptons, of which one is not identified, constitute one of the main backgrounds in the search region bins. In order to reduce this background contribution, we remove events with an isolated track that could stem from leptons that are not well identified but pass the lepton veto. Charged particle tracks from the PV with $p_T > 5\,\text{GeV}$ are selected, and an isolation variable I_{rel} is defined as the p_T sum of all tracks within a cone of $R = 0.3$ around the track candidate (excluding the candidate itself), divided by the track p_T. The isolated tracks considered here come from two different sources, where one is from isolated leptons that satisfy looser ID criteria than lepton candidates, and the other is from isolated charged hadrons. Charged hadron (lepton) candidates are required to satisfy $I_{rel} < 0.1$ (0.2). In case of multiple isolated track candidates in an event, the one with the highest p_T that has the opposite charge with respect to the selected lepton is chosen. Events with such isolated tracks are rejected if the M_{T2} variable [93], calculated from the transverse momenta of the isolated track and the selected lepton, is below 60 (80) GeV for isolated tracks associated with charged hadrons (leptons).

Furthermore, we require $H_T > 500$ GeV and $L_T > 250\,\text{GeV}$. The usage of L_T instead of p_T^{miss} allows the analysis to be not only sensitive to events with high p_T^{miss}, but also to signal events with very small p_T^{miss} but higher lepton p_T. A minimum number of three jets is required for the baseline analysis, and the two highest-p_T jets are required to fulfill $p_T > 80\,\text{GeV}$.

Events are selected exclusively for the multi-b or the zero-b analyses, depending on the number of b-tagged jets in the event. Events in the multi-b analyses are additionally required to contain at least one top tag. The baseline event selection is summarized in Table 1.

Table 1: Baseline event selection.

One good lepton with $p_T > 25\,\text{GeV}$
No veto lepton with $p_T > 10\,\text{GeV}$
No isolated track with $p_T > 5\,\text{GeV}$ with $M_{T2} < 60$ (80) GeV for hadronic (leptonic) tracks
$L_T > 250\,\text{GeV}$
$H_T > 500\,\text{GeV}$
$n_{jet} \geq 3$
Sub-leading jet with $p_T > 80\,\text{GeV}$
$n_b \geq 1$ and $n_t \geq 1$ (multi-b analysis) or $n_b = 0$ (zero-b analysis)

6 Search strategy and background estimation

The central kinematic variable of this analysis is the absolute value of the azimuthal angle $\Delta\phi$ between the p_T of a hypothetical W boson and the lepton

$$\Delta\phi = \sphericalangle(\vec{p}_T^{\,\ell}, \vec{p}_T^{\,W}), \tag{1}$$

where the p_T of the W boson candidate is reconstructed as $\vec{p}_T^{\,W} = \vec{p}_T^{\,\ell} + \vec{p}_T^{\,miss}$. After the baseline event selection, the main backgrounds are leptonically decaying W+jets and semi-leptonic $t\bar{t}$+jets events. These backgrounds contain both one prompt lepton and one neutrino from the

W boson decay in the final state, and are predominantly located at small values of $\Delta\phi$ because of the correlation between the neutrino-related $\vec{p}_{\mathrm{T}}^{\,\mathrm{miss}}$ and the lepton momentum. On the other hand, the SUSY models with two neutralinos in the final state break this correlation, resulting in a nearly uniform distribution in $\Delta\phi$, as shown in Fig. 2.

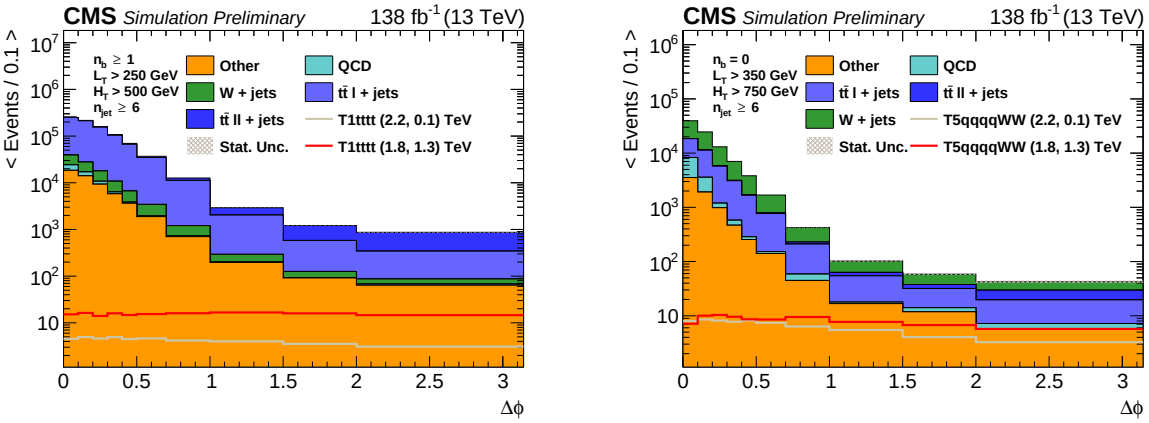

Figure 2: Comparison of signal and background distributions as predicted by simulation in the $\Delta\phi$ variable for (left) the multi-b selection, requiring $n_{\mathrm{jet}} \geq 6$, $L_{\mathrm{T}} > 250\,\mathrm{GeV}$, $H_{\mathrm{T}} > 500\,\mathrm{GeV}$, and (right) the zero-b channel, requiring $n_{\mathrm{jet}} \geq 6$, $L_{\mathrm{T}} > 350\,\mathrm{GeV}$, $H_{\mathrm{T}} > 750\,\mathrm{GeV}$. While most background contributions are at low $\Delta\phi$ values, the signal, shown for two representative combinations of gluino/neutralino masses with large (2.2 TeV/0.1 TeV) and small (1.8 TeV/1.3 TeV) mass difference, is almost flat over the whole range.

The effect of the top quark tagging in the multi-b analysis is shown in Fig. 3 for the sum of all background contributions and for two representative signal models with a gluino/neutralino mass of 2.2 TeV/0.1 TeV and 1.8 TeV/1.3 TeV. While the background in the search region at high $\Delta\phi$ is reduced by an order of magnitude when requiring one top tag, the signal shows almost no reduction. Therefore, one top tag is always required, and a few search region bins are defined to have two or more. When applying W boson tagging with the "tight" working point in the zero-b analysis, the signal is reduced by about 40%, while the W+jets background is reduced by more than 90%. The search region bins are split to contain events with either $n_{\mathrm{W}} = 0$ or $n_{\mathrm{W}} \geq 1$.

The $\Delta\phi$ variable is used to further suppress the background contributions. The region with large $\Delta\phi$ is defined as search region (SR), while small $\Delta\phi$ values are used as control region (CR). For the multi-b analysis, the CR is defined by $\Delta\phi < 0.75$, whereas in the zero-b analysis the $\Delta\phi$ requirement depends on L_{T}. It ranges between 0.5 and 1 and is referred to as $\Delta\phi_0$. This accounts for a possible higher boost of the W boson and correspondingly smaller $\Delta\phi$ at larger values of L_{T}. The search region is split into bins of n_{jet}, n_{b}, L_{T}, and H_{T}, and further categorized by n_{t} (n_{W}) for the multi-b (zero-b) analysis. The different SRs must provide good sensitivity for the different signal models and signal parameters, while providing sufficient statistical accuracy in CRs to predict the background in the corresponding SR. The detailed definitions of all SR bins for the multi-b analysis can be found in Table 7, and for zero-b in Table 8. There is no overlap between the multi-b and zero-b SRs, and they are never used simultaneously, since the results are interpreted in different simplified models.

The principal tool to estimate the background contributions in the search region bins is a transfer factor, called R^{CS}, from CR to SR, which is measured in a sideband with lower jet multiplicity, for each SR bin separately. For this estimation, we split the regions into a low-n_{jet} region, which is called the sideband (SB), and a high-n_{jet} region, which is called the mainband (MB).

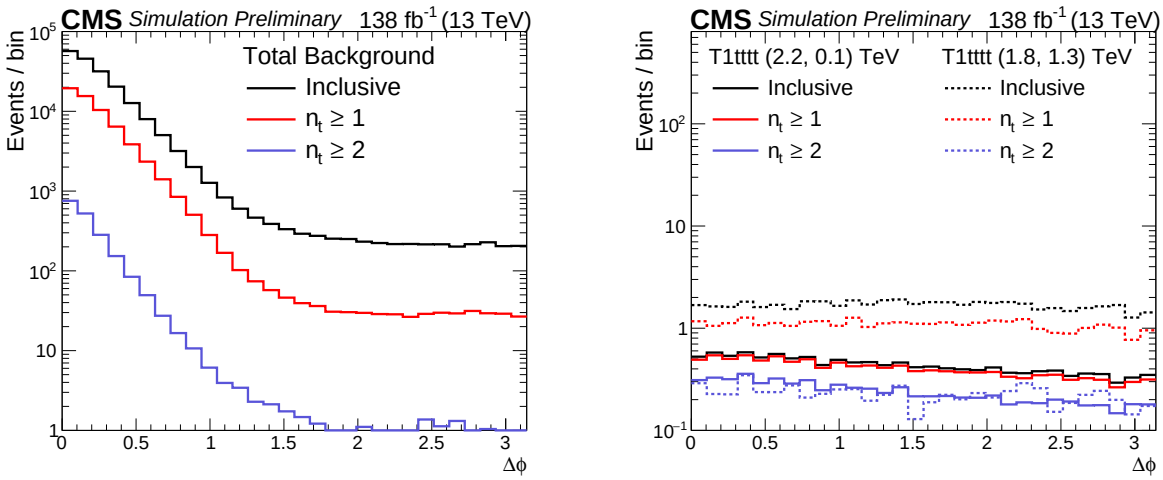

Figure 3: Distributions of $\Delta\phi$ as obtained from simulation showing the impact of top quark tagging after requiring various top-tag multiplicities for (left) the total background and (right) for the signal in two representative combinations of gluino/neutralino masses with large (2.2 TeV/0.1 TeV) and small (1.8 TeV/1.3 TeV) mass difference. After requiring at least one top tag, the background is strongly suppressed, while the efficiency for signal remains high.

Both of these bands are further divided by $\Delta\phi$ into a CR (with low $\Delta\phi$) and a SR (with high $\Delta\phi$) as described above. This method can be considered as a factorization approach in $\Delta\phi$ and jet multiplicity with four regions indexed by CR, SR, SB, and MB. We note that signal contamination in the sidebands is small, and is taken into account in the final interpretation of the result.

To account for possible deviations from the factorization assumption in the extrapolation from SB to MB, we define multiplicative correction factors κ, determined from simulations, as described in Sections 6.1 and 6.2.

In the multi-b analysis, the background is dominated by $\mathrm{t\bar{t}}$ events. In regions with one b-tagged jet and four or five jets, about 80% $\mathrm{t\bar{t}}$ events and 15 to 20% W+jets and single top quark events are expected, while in all other multi-b regions, the $\mathrm{t\bar{t}}$ background contribution is completely dominant. With only one SM process dominating the background contribution, a single R^{CS} factor is defined in the multi-b analysis for each SR bin. The background estimation is explained in detail in Section 6.1.

In the zero-b analysis, backgrounds from $\mathrm{t\bar{t}}$ production are suppressed and contributions from W+jets production are found to be of the same size. Here, an extension of the multi-b strategy is employed, which takes into account differences in the R^{CS} values for these two backgrounds, as detailed in Section 6.2.

An overview of the $(n_{\mathrm{jet}}, n_{\mathrm{b}})$ regions used in this analysis is given in Table 2.

6.1 Background estimate in the multi-b final state

The predicted number $N_{\mathrm{pred}}^{\mathrm{MB,SR}}$ of background events in each MB SR bin is given as the sum of the number of background events from $\mathrm{t\bar{t}}$ and electroweak processes $N_{\mathrm{Pred,EW}}^{\mathrm{MB,SR}}$ and the number of QCD multijet events $N_{\mathrm{Pred,QCD}}^{\mathrm{MB,SR}}$:

$$N_{\mathrm{Pred}}^{\mathrm{MB,SR}} = N_{\mathrm{Pred,EW}}^{\mathrm{MB,SR}} + N_{\mathrm{Pred,QCD}}^{\mathrm{MB,SR}} \,. \tag{2}$$

Table 2: Overview of the definitions of sideband and mainband regions. For the multijet (QCD) fit the electron (e) sample is used, while the muon (μ) sample is used for the determination (det.) of $R^{CS}(W^{\pm})$.

Analysis	Multi-b analysis		Zero-b analysis	
	$n_b = 0$	$n_b \geq 1$	$n_b = 0$	$n_b \geq 1$
$n_{jet} = 3$	QCD bkg. fit (e sample)	R^{CS} det.	R^{CS}(W+jets) det. (μ sample), QCD bkg. fit (e sample)	$R^{CS}(t\bar{t})$ det.
$n_{jet} = 4$				
$n_{jet} = 5$			MB	
$n_{jet} \geq 6$		MB		

The generic label "EW" refers to all backgrounds other than QCD multijet events. About 10 to 15% of the SM background events in the SB CR are expected to be QCD multijet events, while this fraction is significantly smaller in the MB SR. This background contribution is estimated independently from a fit to data as described in Section 6.4. The multijet background is subtracted from the number of background events when calculating the transfer factor R^{CS}_{data} from data:

$$R^{CS}_{data}\Big(n_{jet} \in [4,5]\,, n_b \text{ as in MB}\Big) = \frac{N^{SB,SR}_{data} - N^{SB,SR}_{Pred,QCD}}{N^{SB,CR}_{data} - N^{SB,CR}_{Pred,QCD}}\,. \tag{3}$$

Here, $N^{SB,SR}_{data}$ is the number of events in the SB SR, while $N^{SB,CR}_{data}$ corresponds to the number of events in the SB CR. The independently estimated number of multijet events for these two regions are $N^{SB,SR}_{Pred,QCD}$ and $N^{SB,CR}_{Pred,QCD}$. For the multi-b analysis, the label "n_{jet} as in MB" refers to either ($n_{jet} \in [6,8]$) or ($n_{jet} \geq 9$), depending on the specific search bin.

The SB region, where R^{CS} is determined for each SR bin, is required to have four or five jets, while the MB region must satisfy $n_{jet} \in [6,8]$ or $n_{jet} \geq 9$. This is represented graphically in Fig. 4 (left). At very high H_T, R^{CS} is determined jointly across all three n_b bins to increase the number of events, as the overall uncertainty of the background prediction for several of the search bins is dominated by the statistical uncertainty of the yield in the SB SR.

Small differences in R^{CS} between CR and SR are corrected by the additional factor κ_{EW}, which is determined in simulation as the ratio of the R^{CS} for simulated events:

$$\kappa_{EW} = \frac{R^{CS}_{MC,EW}\Big(n_{jet} \text{ as in MB}\Big)}{R^{CS}_{MC,EW}\Big(n_{jet} \in [4,5]\Big)}\,. \tag{4}$$

The κ_{EW} factor is determined separately for each search bin, except that a common κ_{EW} factor is applied for the $n_b \geq 2$ search bins with the same H_T and L_T, since the κ_{EW} factors are found to be nearly independent of n_b. In general, these correction factors are found to be close to unity. With these definitions, the number of predicted EW events in the MB SR is given by:

$$N^{MB,SR}_{Pred,EW} = \kappa_{EW} R^{CS}_{data}\Big(n_{jet} \in [4,5]\,, n_b \text{ as in MB}\Big)\,\Big(N^{MB,CR}_{data} - N^{MB,CR}_{Pred,QCD}\Big)\,. \tag{5}$$

For semileptonic $t\bar{t}$ events, R^{CS} typically has values of 0.01 to 0.02, depending on the search bin. Similar values, ranging from 0.01 to 0.04, are found for W+jets events. In events with more than one high-p_T neutrino, e.g., in $t\bar{t}$ events in which both W bosons decay leptonically, R^{CS} is higher with values of around 0.5. This is expected, since a large fraction of background events at high $\Delta\phi$ is due to the dileptonic $t\bar{t}$ background, while the low-$\Delta\phi$ region is dominated by events

with only one neutrino. A larger R^{CS} is also expected for events with three neutrinos, such as $t\bar{t}Z$, when the $t\bar{t}$ system decays semileptonically and the Z boson decays to two neutrinos.

Most of the SRs with six or more jets are dominated by semileptonic $t\bar{t}$ events, and therefore this background dominates the total R^{CS} value of about 0.05. As the R^{CS} for dileptonic events, where one lepton is not identified or lost, is an order of magnitude larger than for semileptonic events, we correct the number of genuine dilepton events for this slight difference in the n_{jet} shape measured in dilepton and one-lepton control regions, as explained in more detail in Section 6.3.

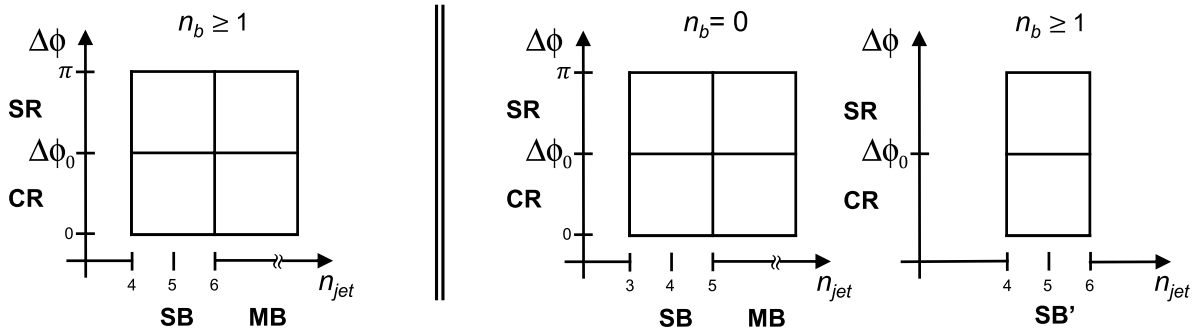

Figure 4: Graphical presentation of the SB, MB, CR, and SR (left) for the multi-b and (middle and right) for the zero-b analysis. The value of $\Delta\phi$ separating CR and SR is labeled as $\Delta\phi_0$. It is constant for the multi-b channel but varies for the zero-b analysis.

6.2 Background estimate in the zero-b final state

Different from the multi-b analysis, where we have only one dominant background in each bin, the search bins in the zero-b analysis require the prediction of two backgrounds of almost the same size, $t\bar{t}$ and W+jets events. These background contributions are estimated by applying the R^{CS} method separately for each of the two components. Since we split these two contributions in the background estimation, we typically have smaller bin counts and consequently larger statistical fluctuations. To guarantee sufficient statistical precision, we perform the prediction for the full Run 2 data set instead of separate estimations for 2016, 2017, and 2018.

This strategy implies the use of two sidebands enriched in W+jets (SB) and $t\bar{t}$ events (SB'), respectively. We decompose the total background in each bin, for example in MB SR, as:

$$N_{\text{Pred}}^{\text{MB,SR}} = N_{\text{Pred,W}}^{\text{MB,SR}} + N_{\text{Pred,}t\bar{t}}^{\text{MB,SR}} + N_{\text{MC,Other}}^{\text{MB,SR}} + N_{\text{Pred,QCD}}^{\text{MB,SR}} \,, \tag{6}$$

where the number of predicted W+jets and $t\bar{t}$ events is denoted by $N_{\text{Pred,W}}^{\text{MB,SR}}$ and $N_{\text{Pred,}t\bar{t}}^{\text{MB,SR}}$, respectively. We also include WW and WZ events, where the W boson decays leptonically and the second W or the Z boson hadronically, as a part of W+jets estimation, since they have similar kinematic properties and R^{CS} values. All other diboson events are treated as part of the rare backgrounds, which are estimated from simulation and denoted by $N_{\text{MC,Other}}^{\text{MB,SR}}$. The small contribution of the QCD multijet background is fixed to the yield estimated from data as described in Section 6.4 and noted as $N_{\text{Pred,QCD}}^{\text{MB,SR}}$.

The $t\bar{t}$ and the W+jets contributions are estimated with an R^{CS} method in a similar way as described in the previous section. The R^{CS} values for W+jets and $t\bar{t}$ events are measured in separate SB regions with different b-jet requirements as laid out in Fig. 4 middle and right.

The value of R^{CS} for $\mathrm{t\bar{t}}$ events is calculated in the multi-b sideband (SB′) with $n_{\mathrm{jet}} \in [4,5]$ and $n_{\mathrm{b}} \geq 1$:

$$R^{\mathrm{CS}}_{\mathrm{data}}\Big(n_{\mathrm{jet}} \in [4,5]\,, n_{\mathrm{b}} \geq 1\Big) = \frac{N^{\mathrm{SB'},\mathrm{SR}}_{\mathrm{data}} - N^{\mathrm{SB'},\mathrm{SR}}_{\mathrm{Pred,QCD}}}{N^{\mathrm{SB'},\mathrm{CR}}_{\mathrm{data}} - N^{\mathrm{SB'},\mathrm{CR}}_{\mathrm{Pred,QCD}}}\,. \tag{7}$$

The correction factor κ_{b} accounts for the difference of $R^{\mathrm{CS}}_{\mathrm{t\bar{t}}}$ between samples with zero b-tagged jets and samples with at least one b-tagged jet and is taken from simulation:

$$\kappa_{\mathrm{b}} = \frac{R^{\mathrm{CS}}_{\mathrm{t\bar{t}}}\left(n_{\mathrm{jet}} \in [4,5]\,, n_{\mathrm{b}} = 0\right)}{R^{\mathrm{CS}}_{\mathrm{EW}}\left(n_{\mathrm{jet}} \in [4,5]\,, n_{\mathrm{b}} \geq 1\right)}, \text{ where } R^{\mathrm{CS}}_{\mathrm{MC}} = \frac{N^{\mathrm{SB'},\mathrm{SR}}_{\mathrm{MC}}}{N^{\mathrm{SB'},\mathrm{CR}}_{\mathrm{MC}}} \text{ and MC} \in [\mathrm{t\bar{t}}, \mathrm{EW}]\,. \tag{8}$$

The factor $\kappa_{\mathrm{t\bar{t}}}$ corrects for a residual dependence of $R^{\mathrm{CS}}_{\mathrm{t\bar{t}}}$ on n_{jet}, in analogy to the κ_{EW} factor defined in Section 6.1. It is defined as:

$$\kappa_{\mathrm{t\bar{t}}} = \frac{R^{\mathrm{CS}}_{\mathrm{t\bar{t}}}\left(n_{\mathrm{jet}} \text{ as in MB}, n_{\mathrm{b}} = 0\right)}{R^{\mathrm{CS}}_{\mathrm{t\bar{t}}}\left(n_{\mathrm{jet}} \in [4,5]\,, n_{\mathrm{b}} = 0\right)}\,. \tag{9}$$

Similar to the multi-b part, the number of simulated dilepton $\mathrm{t\bar{t}}$ events in the factor $\kappa_{\mathrm{t\bar{t}}}$ is corrected by the slight difference in the n_{jet} shape measured in dilepton and one-lepton control regions (see Section 6.3).

Both values, κ_{b} and $\kappa_{\mathrm{t\bar{t}}}$, are close to unity, and statistical uncertainties from the simulation are propagated to the predicted yields.

Finally, the fraction of $\mathrm{t\bar{t}}$ and W+jets events in the MB CR is estimated by a template fit to the n_{b} distribution for each search bin. The number of QCD events in these fits is consistently fixed to the number of events predicted from data as described in Section 6.4, while all other rare backgrounds are taken from simulation and fixed in the fit as well. The templates are taken from simulation. Only the number of $\mathrm{t\bar{t}}$ and W+jets events is adjusted in the fit. The fractions are:

$$f_i^{\mathrm{MB,CR}} = \frac{N^{\mathrm{MB,CR}}_{\mathrm{fit},i}}{N^{\mathrm{MB,CR}}_{\mathrm{data}}}, \text{ with } i \in [\mathrm{t\bar{t}}, \text{W+jets}]\,. \tag{10}$$

The uncertainties in these two components are propagated as systematic uncertainties to the final prediction.

The final $\mathrm{t\bar{t}}$ prediction is:

$$N^{\mathrm{MB,SR}}_{\mathrm{Pred,t\bar{t}}} = \underbrace{\kappa_{\mathrm{b}}\kappa_{\mathrm{t\bar{t}}} R^{\mathrm{CS}}_{\mathrm{data}}\Big(n_b \geq 1, n_{\mathrm{jet}} \in [4,5]\Big)}_{\text{transfer factor}} \underbrace{f^{\mathrm{MB,CR}}_{\mathrm{t\bar{t}}} N^{\mathrm{MB,CR}}_{\mathrm{data}}}_{\mathrm{t\bar{t}} \text{ contribution in the control region}}\,. \tag{11}$$

The W+jets contribution $N^{\mathrm{MB,SR}}_{\mathrm{PredW}}$ is also estimated using an R^{CS} method. The zero-b sideband (SB) is chosen with $n_{\mathrm{jet}} \in [3,4]$, $n_{\mathrm{b}} = 0$. With respect to the SB used for the estimate of $R^{\mathrm{CS}}_{\mathrm{t\bar{t}}}$, a lower jet multiplicity is chosen in order to limit the contamination from $\mathrm{t\bar{t}}$ events. Here we select only events where the lepton is identified as a muon, since this sample has a negligible contamination from QCD multijet events, contrary to the electron channel. A systematic uncertainty is derived from simulation to cover potential differences between the μ and the combined e and μ samples.

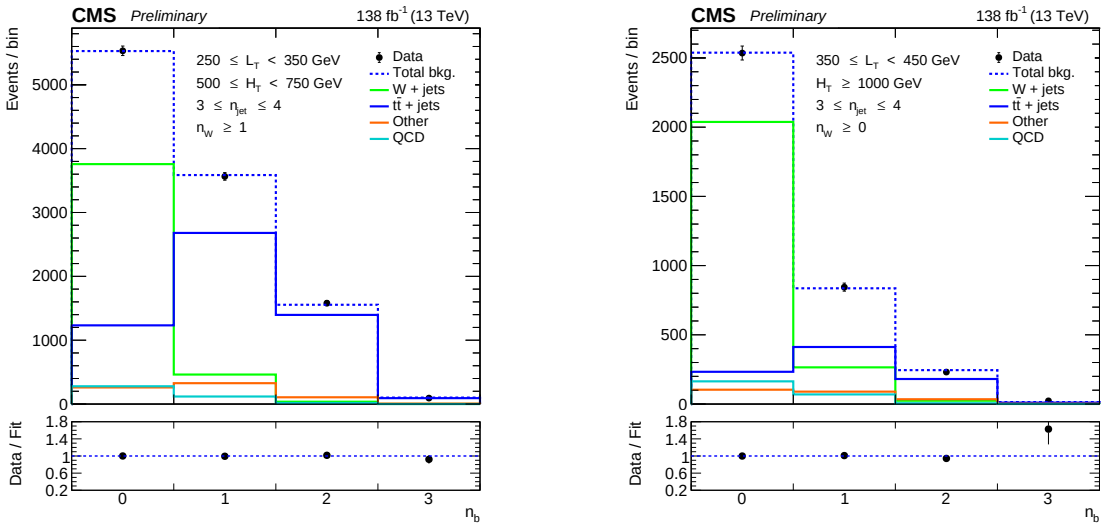

Figure 5: Fits to the n_b multiplicity for control regions for the muon channel and with the requirements (left) $3 \leq n_\mathrm{jet} \leq 4$, $250 < L_\mathrm{T} < 350\,\mathrm{GeV}$, $500 < H_\mathrm{T} < 750\,\mathrm{GeV}$, $n_\mathrm{W} \geq 1$, $\Delta\phi < 1$ and (right) $3 \leq n_\mathrm{jet} \leq 4$, $350 < L_\mathrm{T} < 450\,\mathrm{GeV}$, $H_\mathrm{T} > 1000\,\mathrm{GeV}$, $n_\mathrm{W} \geq 0$, $\Delta\phi < 1$.

The fit of the n_b distribution is also performed in the SB to determine the fraction $f_{\mathrm{t\bar{t}}}^{\mathrm{SB,CR}}$, since the $\mathrm{t\bar{t}}$ contamination is too large to just be ignored. Examples of these fits are shown in Fig. 5.

The $\mathrm{t\bar{t}}$ yields are then subtracted in the numerator and denominator when determining R^CS for the W+jets estimate.

$$R_\mathrm{data}^{\mathrm{CS,\,corr}}\Big(n_\mathrm{jet} \in [3,4]\,, n_\mathrm{b} = 0, n_\mu = 1\Big) = \frac{N_\mathrm{data}^\mathrm{SB,SR} - f_{\mathrm{t\bar{t}}}^{\mathrm{SB,CR}} \kappa_\mathrm{b} R_\mathrm{data}^\mathrm{CS}\Big(n_\mathrm{jet} \in [4,5]\,, n_\mathrm{b} \geq 1\Big) N_\mathrm{data}^\mathrm{SB,CR}}{\Big(1 - f_{\mathrm{t\bar{t}}}^{\mathrm{SB,CR}}\Big) N_\mathrm{data}^\mathrm{SB,CR}}\,. \tag{12}$$

Again, the factor κ_W corrects for a residual dependence of R_W^CS on the jet multiplicity. In addition, it also provides the extrapolation from the muon channel to the electron channel.

$$\kappa_\mathrm{W} = \frac{R_\mathrm{W}^\mathrm{CS}\Big(n_\mathrm{jet}\text{ as in MB}, n_\mathrm{b} = 0, n_\mathrm{l} = 1\Big)}{R_\mathrm{W+Other}^\mathrm{CS}\Big(n_\mathrm{jet} \in [3,4]\,, n_\mathrm{b} = 0, n_\mu = 1\Big)}, \text{ where } R_\mathrm{MC}^\mathrm{CS} = \frac{N_\mathrm{MC}^\mathrm{SB,SR}}{N_\mathrm{MC}^\mathrm{SB,CR}} \text{ and MC} \in [\mathrm{W}, \mathrm{W{+}Other}]\,. \tag{13}$$

The final prediction of the W+jets background is then given by:

$$N_\mathrm{Pred,W}^\mathrm{MB,SR} = \underbrace{\kappa_\mathrm{W} R_\mathrm{data}^{\mathrm{CS,\,corr}}\Big(n_\mathrm{jet} \in [3,4]\,, n_\mathrm{b} = 0, n_\mu = 1\Big)}_{\text{transfer factor}} \underbrace{f_\mathrm{W}^\mathrm{MB,CR} N_\mathrm{data}^\mathrm{MB,CR}}_{\text{W contribution in the control region}}\,. \tag{14}$$

6.3 Dilepton control region correction

The background prediction is sensitive to the extrapolation of R^CS from the low-n_jet SB to the MB regions with higher jet multiplicities. The R^CS values differ significantly for events with only one genuine lepton compared to events with two genuine leptons (mainly dileptonic $\mathrm{t\bar{t}}$), where one lepton is not identified or lost. In the first case, the values are of the order 0.01–0.02, while for dileptonic events the value is around 0.5. In the latter case the $p_\mathrm{T}^\mathrm{miss}$ in the event is not only caused by the neutrino of a leptonically decaying W boson, but also from the second

genuine lepton that is not identified, mostly because it is a hadronically decaying τ lepton leading to more neutrinos in the event, or because it is out of acceptance. This leads to more events in the high $\Delta\phi$ region and a significantly higher R^{CS}. In general, the prediction is not affected by the different R^{CS} of the different processes, if the ratio of events with one genuine lepton to events with two genuine leptons (and one lost or not identified) is the same for all n_{jet} regions.

Small differences can be corrected with an additional n_{jet} dependent correction factor that is applied to genuine simulated dilepton events. The correction factor is based on a double-ratio of a high-purity dilepton control sample and single-lepton events in data. The latter are required to pass the single-lepton baseline selection excluding the SRs.

The high-purity dilepton events are transformed artificially into typical single-lepton events by removing the second lepton as described in the following. The dilepton control sample is selected by requiring two leptons of opposite charge. In order to reduce the DY background in the multi-b analysis, the invariant mass of same-flavor leptons is required to be more than 10 GeV away from the Z boson mass peak. For the zero-b selection, where the DY background is more important because of the 0 b-tag requirement, we allow only two leptons of different flavor. To simulate the feed-down of the dileptonic events into the single-lepton selection, one of the two leptons is removed from the event. Since these "lost leptons" are mainly from $\tau \to$ hadrons + ν decays, we replace the removed lepton with a jet with 2/3 of the original lepton's p_{T} to model the typical visible energy of a τ lepton, accommodating for the missing momentum due to the neutrino from the τ decay. In the next step L_{T}, $\Delta\phi$, and H_{T} values of the now "single-lepton" event (with the additional "jet") are recalculated. In order to maximize the number of events, no $\Delta\phi$ requirement is applied, and all events are used twice, with each reconstructed lepton being considered as the lost lepton.

In the events with one genuine lepton in the zero-b selection, a change in the background composition (mainly $\mathrm{t\bar{t}}$ and W+jets) could lead to a change of the correction factor. The size of this additional change is hard to determine and it is desirable to disentangle these two effects. In order to tackle this issue, we normalize these two backgrounds using weights extracted after performing the template fit on the b-tag multiplicity.

The correction factor is determined as a function of n_{jet} for each event from a linear fit to the double-ratio between data over MC yields for dilepton (transformed to "single-lepton") and single-lepton events of the form:

$$w_{\mathrm{DL}} = a + b(n_{\mathrm{jet}} - \langle n_{\mathrm{jet}} \rangle), \tag{15}$$

where a is the constant, b is the slope, and $\langle n_{\mathrm{jet}} \rangle$ is the weighted mean. The correction factor is applied as a weight to all simulated events that are flagged as dileptonic from generator level information.

As an example, the jet multiplicity distribution as well as the double-ratio for 2018 data is shown in Fig. 6 after the single-lepton baseline selection (excluding the SRs) and the dilepton CRs for the multi-b and for the zero-b selection.

The systematic variations around that new central value are determined by varying the fit to the double-ratio by the following uncertainties: the variation of the constant value a is extracted as the quadratic sum of the deviation of the central value of a from unity and by the uncertainty in a that is extracted from the fit itself. The variation of the slope b is determined as the quadratic sum of the deviation of b from zero and the uncertainty in b as given by the fit.

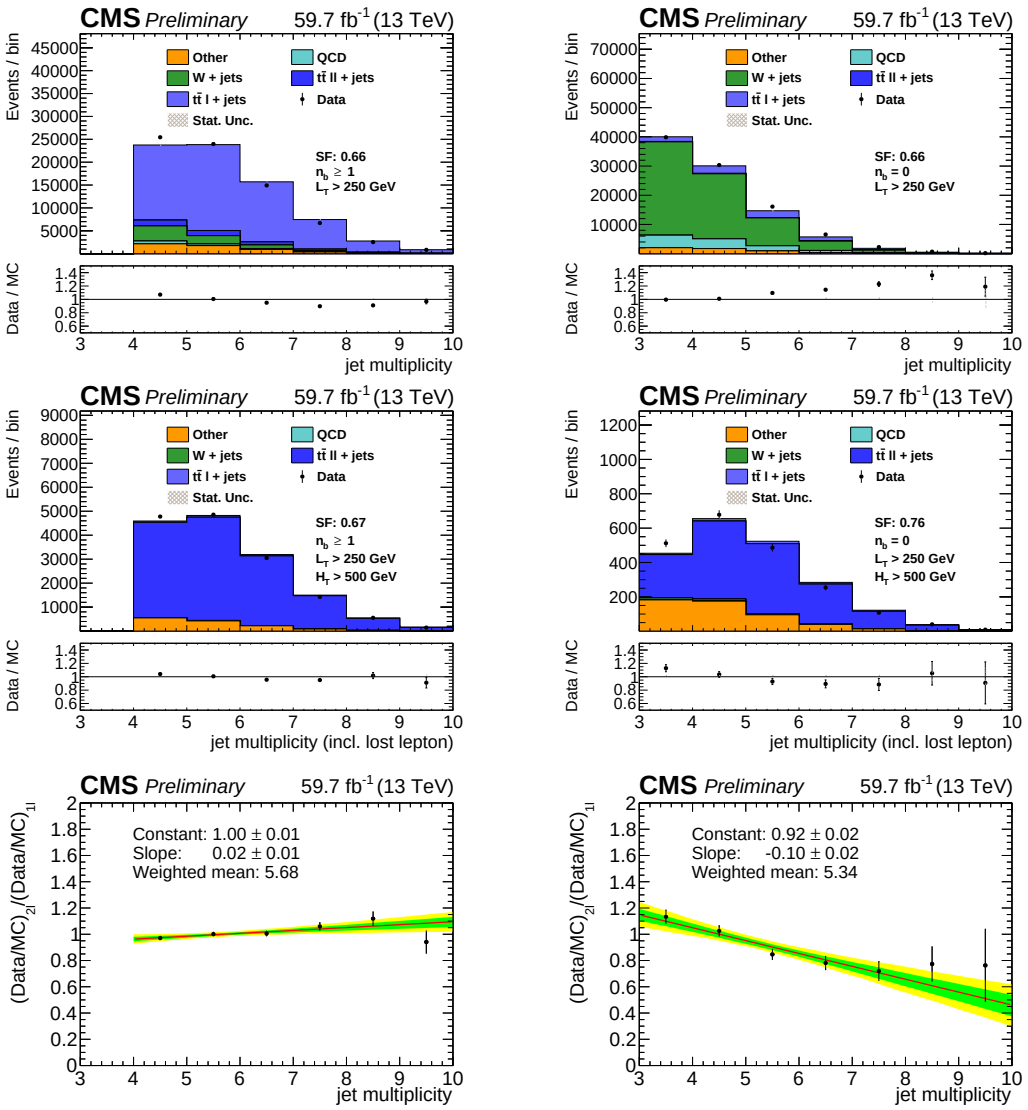

Figure 6: The top row shows the jet multiplicity distribution after the single-lepton baseline selection excluding the SRs (left) for the multi-b selection and (right) for the zero-b selection, while the middle row contains the dilepton CRs, again (left) for the multi-b selection and (right) for the zero-b selection. The simulation is normalized to data with the scale factor (SF) mentioned in the plot. The double ratio of the single-lepton and dilepton ratio between data and simulation together with the fit is shown in the bottom row for (left) the multi-b and (right) the zero-b analysis. The fits are performed for each data taking year, 2018 is shown as an example.

6.4 Estimation of QCD multijet background

The QCD multijet events that pass the event selection typically have a reconstructed electron that originates from misidentified jets or from photon conversions in the inner detector. This background contribution is estimated from the yield of "anti-selected" electron candidates that pass looser identification and isolation requirements and fail the tighter criteria for selected electrons. Muons contribute naturally much less to this background, but are nevertheless studied in the same way. The transfer factor $F_{\text{sel-to-anti}}$ from the anti-selected to the selected lepton sample is extracted in a multijet-enriched control sample with zero b-tagged jets and three or four other jets and therefore fewer prompt leptons.

The estimation method applied here is very similar to the procedure developed in previous CMS analyses [94, 95]. It relies on the L_{P} variable, which reflects the effective lepton polarization in the W decay, defined as:

$$L_{\text{P}} = \frac{p_{\text{T}}^{\ell}}{p_{\text{T}}^{\text{W}}} \cos(\Delta\phi). \tag{16}$$

Here, $\Delta\phi$ is again the angle between the transverse components of lepton and reconstructed W as defined in Eq. (1). According to the simulation, the selected lepton events comprise a mixture of EW and QCD backgrounds. In contrast, the anti-selected electron events are clearly dominated by QCD, as intended by the modified electron identification requirements. As shown in Fig. 7 for the electron channel, the EW background peaks around $L_{\text{P}} = 0$ and falls off towards higher values of L_{P}, while the QCD background peaks around unity.

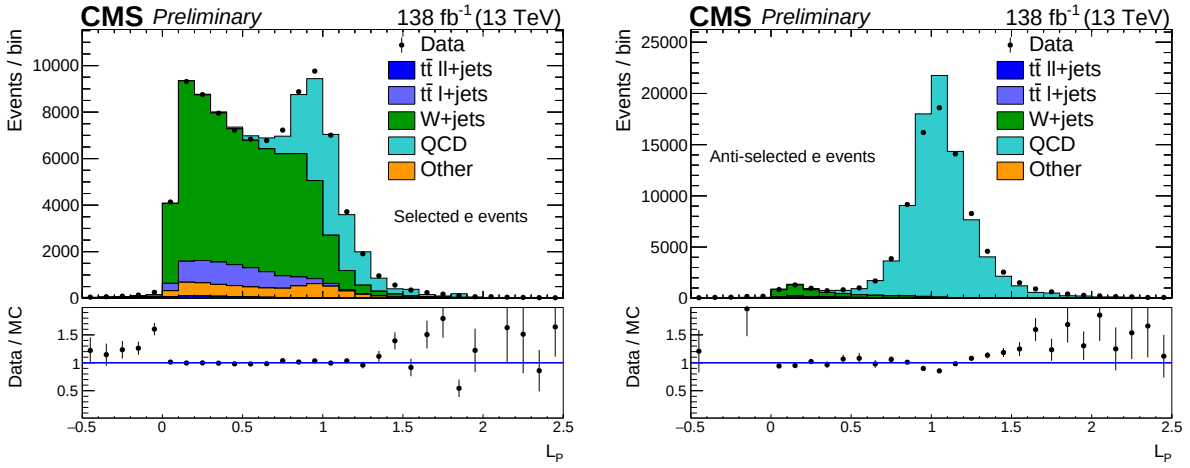

Figure 7: The L_{P} distribution for (left) selected and (right) anti-selected electron candidates in the baseline QCD selection, with modified requirements of $n_{\text{jet}} \in [3,4]$ and $n_{\text{b}} = 0$.

Therefore, the number of EW and QCD events can be determined with template fits in L_{P} to the selected and to the anti-selected lepton candidates. The shape of the templates is taken from the corresponding simulated samples. The ratio of QCD events in selected to anti-selected lepton events is then determined from data requiring zero b tags and three or four jets:

$$F_{\text{sel-to-anti}}\Big(n_{\text{b}} = 0, n_{\text{jet}} \in [3,4]\Big) = \frac{N^{\text{fit, data}}_{\text{QCD selected}}\Big(L_{\text{T}}, n_{\text{b}} = 0, n_{\text{jet}} \in [3,4]\Big)}{N^{\text{fit, data}}_{\text{QCD anti-selected}}\Big(L_{\text{T}}, n_{\text{b}} = 0, n_{\text{jet}} \in [3,4]\Big)}\,. \tag{17}$$

This ratio is calculated in bins of L_{T}, but inclusively in H_{T}, since the probability to fake electrons is expected to be largely independent on the number of jets and H_{T}. Typically, the $F_{\text{sel-to-anti}}$

varies between 0.2 for smaller and 0.3 for large values of L_T. This ratio is finally used to predict the QCD background for the search region bins with higher (b) jet multiplicities bin by bin:

$$N^{\text{pred}}_{\text{QCD selected}}\Big(n_{\text{jet}}, n_{\text{b}}\Big) = F_{\text{sel-to-anti}}\Big(n_{\text{b}} = 0, n_{\text{jet}} \in [3,4]\Big)\, N^{\text{data}}_{\text{QCD anti-selected}}\Big(n_{\text{jet}}, n_{\text{b}}\Big)\,. \quad (18)$$

7 Systematic uncertainties

Our search results are subject to various systematic uncertainty sources related to the experimental apparatus and theoretical models. The uncertainties can influence the background and/or modify the expected signal yield. The impact of the uncertainties is evaluated individually for the multi-b and the zero-b analysis, and also separately for the $t\bar{t}$ and W+jets background predictions in the zero-b analysis. The results are summarized in Tables 3 and 4, respectively. In addition, the impact on the yields for two representative signal points for each analysis are shown in Tables 5 and 6.

Table 3: Summary of systematic uncertainties in the background prediction for the multi-b analysis. For each uncertainty source, the median, minimal (min), and maximal (max) impact on the total background prediction is shown, where the three quantities refer to the set of MB SR bins.

Uncertainty source	Total background median [min, max] [%]
Jet energy corrections	3.8 [0.2, 36.3]
QCD multijet	3.8[0.8, 71.0]
$t\bar{t}$V cross sections	2.8 [0.1, 22.6]
ISR modeling	2.3 [0.4, 20.3]
Pileup modeling	2.3 [0.1, 18.6]
Dileptonic correction	2.2 [0.4, 12.3]
$t\bar{t}$ cross section	1.6 [0.1, 23.7]
W+jets polarization	0.6 [0.1, 4.4]
b tagging (efficiency)	0.6 [0.1, 5.7]
W+jets cross section	0.4 [0.1, 7.7]
b tagging (misidentification)	0.3 [0.1, 8.4]
Lepton efficiency	0.2 [0.1, 1.6]

One common large systematic uncertainty is given by the jet energy corrections, which are changed by their uncertainty [88] as a function of jet p_T and η, and these changes are propagated to all observables. The scale factors related to the efficiencies for identifying b quark jets, and the misidentification of the c quark, light quark, or gluon jets are scaled up and down according to their uncertainties. Uncertainties for the efficiency of lepton reconstruction and identification are handled in the same way. The uncertainty in the pileup is determined by varying the inelastic pp cross-section by $\pm 5\%$. All these uncertainties apply to both the background prediction and the signal yield.

The integrated luminosities of the 2016, 2017, and 2018 data-taking periods are individually measured with uncertainties in the 1.2–2.5% range [96–98], while the total Run 2 integrated luminosity has an uncertainty of 1.6%.

The polarization of W bosons is changed by reweighting events by the factor $w = 1 + \alpha(1 - \cos\theta^*)^2$, where θ^* is the angle between the charged lepton and W boson in the W boson rest

Table 4: Summary of systematic uncertainties in the background prediction for the zero-b analysis. For each uncertainty source, the median, minimal (min), and maximal (max) impact on the $t\bar{t}$, W+jets, and total background prediction is shown, where the three quantities refer to the set of MB SR bins.

Uncertainty source	$t\bar{t}$ median [min, max] [%]	W+jets median [min, max] [%]	Total background median [min, max] [%]
QCD multijet	—	—	5.2 [1.5, 27.6]
$t\bar{t}V$ cross sections	0.9 [0.2, 5.3]	0.3 [0.1, 2.1]	4.0 [1.0, 19.6]
Jet energy corrections	1.4 [0.1, 34.4]	1.2 [0.1, 22.0]	3.5 [0.5, 40.5]
Pileup modeling	0.5 [0.1, 5.5]	0.6 [0.1, 4.8]	1.2 [0.1, 13.1]
Dileptonic correction	2.0 [0.2, 13.7]	0.1 [0.1, 0.9]	0.8 [0.1, 4.7]
W+jets cross section	0.6 [0.1, 2.6]	1.5 [0.1, 13.7]	0.7 [0.1, 4.5]
b tagging (efficiency)	0.3 [0.1, 2.7]	0.1 [0.1, 1.8]	0.6 [0.2, 4.6]
W+jets polarization	0.2 [0.1, 2.9]	0.8 [0.1, 7.6]	0.4 [0.1, 4.1]
Lepton efficiency	0.1 [0.1, 1.4]	0.1 [0.1, 1.6]	0.4 [0.1, 2.3]
$t\bar{t}$ cross section	1.3 [0.1, 10.3]	—	0.3 [0.1, 3.2]
Luminosity	—	—	0.3 [0.1, 1.0]
ISR modeling	0.5 [0.1, 14.1]	—	0.1 [0.1, 4.4]
b tagging (misidentification)	0.1 [0.1, 0.5]	0.1 [0.1, 0.3]	0.1 [0.1, 0.7]

Table 5: Summary of systematic uncertainties in the signal prediction for the multi-b analysis. For each uncertainty source, the median, minimal (min), and maximal (max) impact on the total background prediction is shown, where the three quantities refer to the set of MB SR bins. The MET uncertainty has a very high maximum value for T1tttt$(2.2, 0.1)$ in one bin with low sensitivity to the signal. The gluino and LSP masses are indicated in units of TeV.

Uncertainty source	T1tttt$(1.8, 1.3)$ TeV median [min, max] [%]	T1tttt$(2.2, 0.1)$ TeV median [min, max] [%]
Top quark tagging	10.0 [10.0, 10.0]	10.0 [10.0, 10.0]
Jet energy corrections	10.4 [0.1, 62.0]	8.8 [0.1, 58.8]
$p_{\mathrm{T}}^{\mathrm{miss}}$	8.4 [1.0, 73.3]	4.2 [0.1, 129.2]
ISR modeling	4.7 [0.1, 50.9]	6.2 [0.1, 27.1]
b tagging (efficiency)	4.6 [0.1, 15.9]	7.3 [0.1, 26.9]
Luminosity	1.6 [1.6, 1.6]	1.6 [1.6, 1.6]
b tagging (misidentification)	0.5 [0.1, 8.9]	0.6 [0.1, 7.4]

frame. In W+jets events, we take α to be 0.1, guided by the theoretical uncertainty and measurements found in Refs. [94, 99–101]. For $t\bar{t}$+jets events, we take $\alpha = 0.05$. For W+jets events, where the initial state can have different polarizations for W^+ and W^- bosons, we take as uncertainty the larger change in κ resulting from reweighting only the W^+ bosons in the sample, and from reweighting all W bosons.

While the W+jets and $t\bar{t}$ backgrounds are estimated from data, a change in their relative contribution can lead to changes in the R^{CS} at low jet multiplicities of the sideband. Therefore, the inclusive W+jets and $t\bar{t}$ cross sections are conservatively varied by 30% above and below the nominal value to account for possible biases in the estimation of the background composition. The small contribution of $t\bar{t}$ produced with an additional vector boson ($t\bar{t}V$) is conservatively varied by 100% to account for the uncertainty in the theoretical prediction. Final states with $t\bar{t}$ and a vector boson contribute because of their similarity to our signals, where we assume a 100% uncertainty in the cross section. Uncertainties in the signal cross section are shown as

Table 6: Summary of systematic uncertainties in the signal prediction for the zero-b analysis. For each uncertainty source, the median, minimal (min), and maximal (max) impact on the total background prediction is shown, where the three quantities refer to the set of MB SR bins. The gluino and LSP masses are indicated in units of TeV.

Uncertainty source	T5qqqqWW(1.8, 1.3) TeV median [min, max] [%]	T5qqqqWW(2.2, 0.1) TeV median [min, max] [%]
W boson tagging	10.0 [10.0, 10.0]	10.0 [10.0, 10.0]
Jet energy corrections	6.2 [0.8, 72.5]	5.1 [0.1, 50.0]
$p_{\mathrm{T}}^{\mathrm{miss}}$	4.0 [0.1, 28.4]	4.9 [0.1, 63.9]
Luminosity	1.6 [1.6, 1.6]	1.6 [1.6, 1.6]
ISR modeling	1.8 [0.1, 11.3]	1.7 [0.1, 14.8]
b tagging (efficiency)	0.5 [0.2, 5.9]	1.3 [0.2, 6.0]
b tagging (misidentification)	0.2 [0.1, 0.9]	0.4 [0.1, 1.1]

explicit variations of the mass limits (Section 9).

The factorization and renormalization scales are each changed by a factor of 0.5 and 2, leading to varying event yields in simulation. Depending on the jet multiplicity, an uncertainty of 15–50% is applied to the QCD background estimate.

Since we consider a signal with multiple top quarks (W bosons) in the multi-b (zero-b) analysis, the related tagging uncertainties had been investigated carefully. The taggers are described in detail in Section 4. The background estimation is not sensitive to details of the top and W tagging performance, therefore a systematic uncertainty is only assigned for the signal efficiency. The systematic uncertainties in the top quark tagging efficiency and mistagging rate are estimated as follows: The relative yields of events with different top tag multiplicities are used to extract an overall efficiency and mistagging rate. A difference of 5% is observed, and the systematic uncertainty is conservatively taken to be twice this quantity, namely 10%. For W boson tagging, the efficiency and mistagging rates are extracted from a full comparison of data and simulation. A total uncertainty of 10% is found to account for all differences between data and simulation.

The SF applied to correct the ISR in signal samples and 2016 $\mathrm{t\bar{t}}$ is varied by 4–5% (Section 3).

8 Results

A comparison of the observed data yields and the predicted background contributions for the multi-b analysis is given in Table 7 and shown in Fig. 8 for the SR MB for the combination of all three years. Good agreement is observed for almost all search bins. Only in the last bin are two events observed, with only 0.24 ± 0.16 events expected.

Table 8 and Fig. 9 contain the background prediction for the zero-b analysis compared to the data yields in the MB SR. Here, we observe good agreement in almost all bins as well, and a deviation from the prediction is just observed for bins that are dominated by the background. This is caused by fluctuations in the SB used to determine the transfer factor R^{CS} from the CR to the SR.

Table 7: Observed number of events in the search region bins of the multi-b analysis, together with the predicted yields for background and two T1tttt $(m_{\tilde{g}}, m_{\tilde{\chi}_1^0})$ signal points. For the latter, the gluino and LSP masses are indicated in units of TeV. All bins are defined with $\Delta\phi > 0.75$.

n_{jet}	n_{b}	L_{T} [GeV]	H_{T} [GeV]	n_{t}	Bin name	T1tttt signal events		Predicted	Observed
						(1.8, 1.3) TeV	(2.2, 0.1) TeV	background events	events
[6, 8]	1	[250, 450]	[500, 1500]	1	A1a	1.2 ± 0.1	<0.1	576 ± 29	570
				≥ 2	A1b	0.07 ± 0.02	<0.1	13 ± 2	14
			≥ 1500	1	A2a	<0.1	0.01 ± 0.01	47 ± 7	42
				≥ 2	A2b	<0.1	0.04 ± 0.01	5 ± 1	3
		[450, 600]	≥ 500	1	A3a	0.44 ± 0.06	0.04 ± 0.01	31 ± 6	16
				≥ 2	A3b	0.03 ± 0.02	0.06 ± 0.01	1.0 ± 0.3	1
		≥ 600	≥ 500	1	A4a	0.18 ± 0.04	0.44 ± 0.02	7 ± 2	8
				≥ 2	A4b	<0.1	0.48 ± 0.02	1.0 ± 0.5	0
	2	[250, 450]	[500, 1500]	1	B1a	2.3 ± 0.1	0.01 ± 0.01	532 ± 26	586
				≥ 2	B1b	0.28 ± 0.04	0.01 ± 0.01	16 ± 2	19
			≥ 1500	1	B2a	<0.1	0.03 ± 0.01	30 ± 5	34
				≥ 2	B2b	<0.1	0.06 ± 0.01	3.4 ± 0.8	1
		[450, 600]	≥ 500	1	B3a	1.0 ± 0.1	0.07 ± 0.01	27 ± 6	34
				≥ 2	B3b	0.06 ± 0.02	0.09 ± 0.01	1.1 ± 0.5	2
		≥ 600	≥ 500	1	B4a	0.37 ± 0.05	0.67 ± 0.03	6.2 ± 1.6	6
				≥ 2	B4b	0.07 ± 0.02	0.80 ± 0.03	0.23 ± 0.08	0
	≥ 3	[250, 450]	[500, 1500]	1	C1a	3.0 ± 0.1	0.01 ± 0.01	115 ± 7	105
				≥ 2	C1b	0.43 ± 0.06	<0.1	6 ± 1	3
			≥ 1500	1	C2a	0.01 ± 0.01	0.03 ± 0.01	7 ± 2	10
				≥ 2	C2b	<0.1	0.07 ± 0.01	1.0 ± 0.4	2
		[450, 600]	≥ 500	1	C3a	1.1 ± 0.1	0.06 ± 0.01	5 ± 1	4
				≥ 2	C3b	0.24 ± 0.04	0.10 ± 0.01	0.63 ± 0.43	0
		≥ 600	≥ 500	1	C4a	0.42 ± 0.05	0.67 ± 0.02	1.4 ± 0.4	4
				≥ 2	C4b	0.05 ± 0.02	0.76 ± 0.03	0.05 ± 0.04	0
≥ 9	1	[250, 450]	[500, 1500]	1	D1a	0.62 ± 0.06	<0.1	32 ± 3	26
				≥ 2	D1b	0.12 ± 0.03	<0.1	2.1 ± 0.6	4
			≥ 1500	1	D2a	0.02 ± 0.01	0.01 ± 0.01	6 ± 1	11
				≥ 2	D2b	0.02 ± 0.01	0.02 ± 0.01	1.0 ± 0.3	2
		[450, 600]	≥ 500	≥ 1	D3	0.34 ± 0.05	0.04 ± 0.01	2.3 ± 0.6	2
		≥ 600	≥ 500	≥ 1	D4	0.23 ± 0.04	0.40 ± 0.02	0.6 ± 0.3	0
	2	[250, 450]	[500, 1500]	1	E1a	1.5 ± 0.1	0.01 ± 0.01	35 ± 3	35
				≥ 2	E1b	0.55 ± 0.06	<0.1	3.2 ± 0.7	2
			≥ 1500	1	E2a	0.05 ± 0.02	0.02 ± 0.01	8 ± 2	6
				≥ 2	E2b	0.04 ± 0.02	0.05 ± 0.01	1.0 ± 0.4	2
		[450, 600]	≥ 500	1	E3a	0.75 ± 0.07	0.04 ± 0.01	1.7 ± 0.5	1
				≥ 2	E3b	0.19 ± 0.03	0.06 ± 0.01	0.2 ± 0.1	0
		≥ 600	≥ 500	1	E4a	0.50 ± 0.05	0.30 ± 0.02	0.9 ± 0.4	1
				≥ 2	E4b	0.21 ± 0.04	0.55 ± 0.02	0.06 ± 0.04	0
	≥ 3	[250, 450]	[500, 1500]	1	F1a	3.2 ± 0.1	0.01 ± 0.01	13 ± 2	7
				≥ 2	F1b	1.27 ± 0.08	<0.1	2.4 ± 0.8	2
			≥ 1500	1	F2a	0.04 ± 0.02	0.03 ± 0.01	4 ± 1	0
				≥ 2	F2b	0.07 ± 0.02	0.09 ± 0.01	0.7 ± 0.3	0
		[450, 600]	≥ 500	≥ 1	F3	1.7 ± 0.1	0.16 ± 0.01	1.1 ± 0.4	2
		≥ 600	≥ 500	≥ 1	F4	1.0 ± 0.1	1.30 ± 0.03	0.2 ± 0.2	2

Table 8: Observed number of events in the search region bins of the zero-b analysis, together with the predicted yields for background and two T5qqqqWW $(m_{\tilde{g}}, m_{\tilde{\chi}_1^0})$ signal points. For the latter, the gluino and LSP masses are indicated in units of TeV.

n_{jet}	L_{T} [GeV]	H_{T} [GeV]	$\Delta\phi$	n_{W}	Bin name	T5qqqqWW signal events		Predicted background events	Observed events
						(1.8, 1.3) TeV	(2.2, 0.1) TeV		
5	[250, 350]	[500, 750]	>1	0	G0a	1.2 ± 0.1	<0.1	342 ± 24	333
				≥1	G0b	0.46 ± 0.08	<0.1	70 ± 8	77
		750		0	G1a	0.35 ± 0.07	0.03 ± 0.01	292 ± 22	304
				≥1	G1b	0.14 ± 0.04	0.02 ± 0.01	69 ± 10	62
	[350, 450]	[500, 750]	>1	0	G2a	1.8 ± 0.2	<0.1	71 ± 8	63
				≥1	G2b	0.60 ± 0.09	<0.1	14 ± 5	25
		750		0	G3a	0.44 ± 0.08	0.04 ± 0.01	66 ± 8	44
				≥1	G3b	0.24 ± 0.06	0.03 ± 0.01	14 ± 4	13
	[450, 650]	[500, 750]	>0.75	0	G4a	2.1 ± 0.2	<0.1	52 ± 7	45
				≥1	G4b	1.1 ± 0.1	<0.1	12 ± 3	9
		[750, 1250]		0	G5a	0.9 ± 0.1	0.03 ± 0.01	42 ± 6	35
				≥1	G5b	0.35 ± 0.07	<0.1	10 ± 3	6
		≥1250		0	G6a	<0.1	0.17 ± 0.02	16 ± 3	19
				≥1	G6b	<0.1	0.13 ± 0.02	3 ± 1	3
	≥650	[500, 1250]	>0.5	0	G7a	1.3 ± 0.1	0.13 ± 0.02	33 ± 8	32
				≥1	G7b	0.30 ± 0.06	0.04 ± 0.01	7 ± 2	8
		≥1250		0	G8a	0.15 ± 0.05	1.78 ± 0.07	11 ± 3	8
				≥1	G8b	0.04 ± 0.02	1.08 ± 0.05	0.6 ± 0.4	2
[6, 7]	[250, 350]	[500, 1000]	>1	0	H1a	2.6 ± 0.2	<0.1	281 ± 22	292
				≥1	H1b	1.3 ± 0.1	<0.1	71 ± 9	71
		≥1000		0	H2a	0.23 ± 0.06	0.05 ± 0.01	121 ± 11	121
				≥1	H2b	0.18 ± 0.05	0.02 ± 0.01	29 ± 5	21
	[350, 450]	[500, 1000]	>1	0	H3a	3.1 ± 0.2	<0.1	51 ± 6	71
				≥1	H3b	1.6 ± 0.2	0.01 ± 0.01	12 ± 3	15
		≥1000		0	H4a	0.31 ± 0.07	0.09 ± 0.01	31 ± 7	21
				≥1	H4b	0.12 ± 0.04	0.08 ± 0.01	6 ± 2	6
	[450, 650]	[500, 750]	>0.75	0	H5a	3.1 ± 0.2	<0.1	19 ± 4	17
				≥1	H5b	1.6 ± 0.2	<0.1	5 ± 2	9
		[750, 1250]		0	H6a	2.8 ± 0.2	0.01 ± 0.01	29 ± 4	18
				≥1	H6b	1.4 ± 0.1	<0.1	7 ± 2	4
		≥1250		0	H7a	0.4 ± 0.07	0.45 ± 0.03	15 ± 3	14
				≥1	H7b	0.2 ± 0.05	0.33 ± 0.03	3 ± 1	1
	≥650	[500, 1250]	>0.5	0	H8a	2.5 ± 0.2	0.09 ± 0.01	13 ± 3	17
				≥1	H8b	0.9 ± 0.1	0.05 ± 0.01	4 ± 1	4
		≥1250		0	H9a	0.8 ± 0.1	3.9 ± 0.1	9 ± 3	6
				≥1	H9b	0.34 ± 0.07	2.44 ± 0.08	2 ± 1	1
≥8	[250, 350]	[500, 1000]	>1	0	I1a	0.8 ± 0.1	<0.1	23 ± 5	25
				≥1	I1b	0.33 ± 0.07	<0.1	7 ± 3	5
		≥1000		0	I2a	0.30 ± 0.07	0.04 ± 0.01	22 ± 5	23
				≥1	I2b	0.16 ± 0.05	0.01 ± 0.01	8 ± 2	12
	[350, 450]	[500, 1000]	>1	0	I3a	0.8 ± 0.1	<0.1	3.0 ± 0.7	10
				≥1	I3b	0.36 ± 0.07	<0.1	1.1 ± 0.4	0
		≥1000		0	I4a	0.57 ± 0.09	0.07 ± 0.01	5 ± 1	5
				≥1	I4b	0.36 ± 0.07	0.06 ± 0.01	3 ± 1	2
	[450, 650]	[500, 1250]	>0.75	0	I5a	1.5 ± 0.1	<0.1	3.4 ± 0.9	4
				≥1	I5b	1.0 ± 0.1	<0.1	0.5 ± 0.3	1
		≥1250		0	I6a	0.40 ± 0.07	0.26 ± 0.03	2.6 ± 0.8	2
				≥1	I6b	0.18 ± 0.05	0.17 ± 0.02	0.5 ± 0.3	2
	≥650	[500, 1250]	>0.5	≥0	I7	1.4 ± 0.1	0.02 ± 0.01	1.5 ± 0.6	2
		≥1250			I8	1.4 ± 0.1	3.58 ± 0.09	1.5 ± 0.7	1

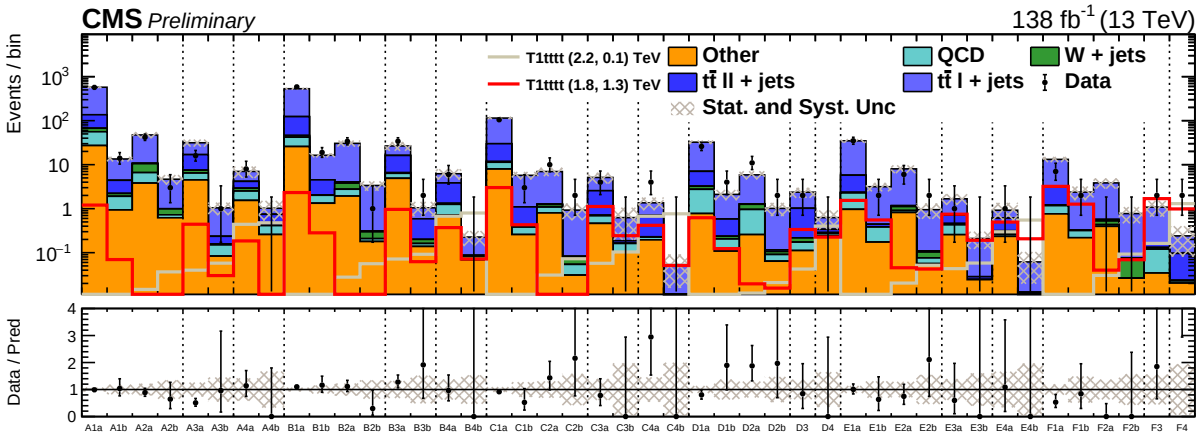

Figure 8: Observed event yields in the MB SR of the multi-b analysis compared to signal and background predictions, for all three years combined. The relative fraction of the different SM EW background contributions determined in simulation is shown by the stacked, colored histograms, normalized so that their sum is equal to the background estimated using data control regions. The QCD background is predicted using the L_P method. The signal is shown for two representative combinations of gluino/neutralino masses with large (2.2 TeV/0.1 TeV) and small (1.8 TeV/1.3 TeV) mass differences.

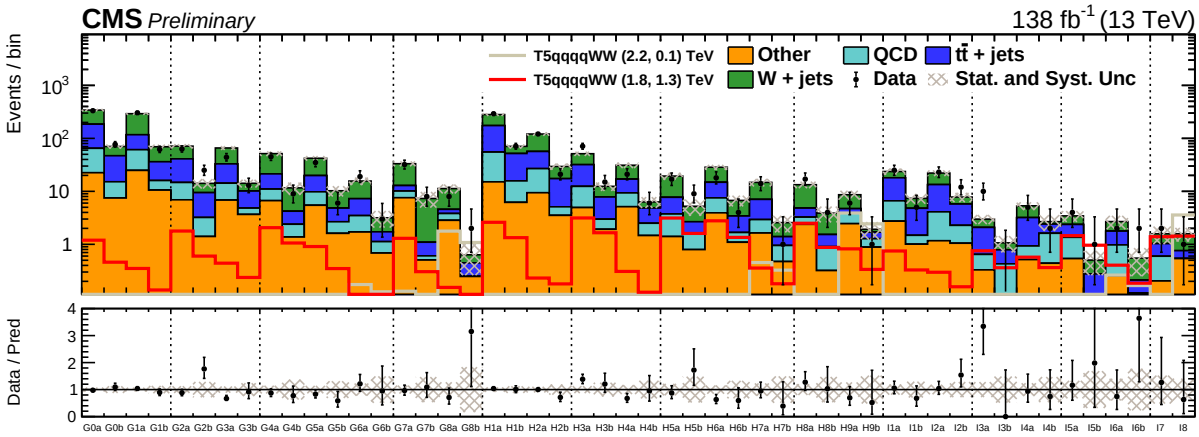

Figure 9: Observed event yields in the MB SR of the zero-b analysis compared to signal and background predictions, for all three years combined. The W+jets, $t\bar{t}$, and QCD predictions are extracted from data control samples, while the other background contributions are estimated from simulation. The signal is shown for two representative combinations of gluino/neutralino masses with large (2.2 TeV/0.1 TeV) and small (1.8 TeV/1.3 TeV) mass differences.

9 Interpretation

We observe good agreement of the data with the background prediction, and set upper limits on the production cross section at 95% confidence level (CL). These are estimated in asymptotic approximation [102] using the modified frequentist CL_s method [103, 104]. The $\tilde{g}\tilde{g}$ pair production cross section calculated at approximate NNLO and NNLL accuracy, and exclusion limits are set as a function of the $(m_{\tilde{g}}, m_{\tilde{\chi}_1^0})$ hypothesis.

For the T1tttt model, which describes gluino pair production with each gluino decaying to a $t\bar{t}$ pair and a $\tilde{\chi}_1^0$, the cross section limits are obtained using the multi-b analysis. They are shown in Fig. 10 (left) as a function of $m_{\tilde{g}}$ and $m_{\tilde{\chi}_1^0}$, assuming branching fractions of 100%. The

observed limit is about one standard deviation lower than the expected one, which is caused by the observation of two events in the last bin, while only 0.24 ± 0.16 events are expected.

The results of the zero-b analysis are interpreted in the T5qqqqWW model, in which pair-produced gluinos decay to a (light) quark-antiquark pair and a chargino, which further decays to a W boson and the $\widetilde{\chi}_1^0$. The observed limit, shown in Fig. 10, agrees with the expected limit over most of the mass range.

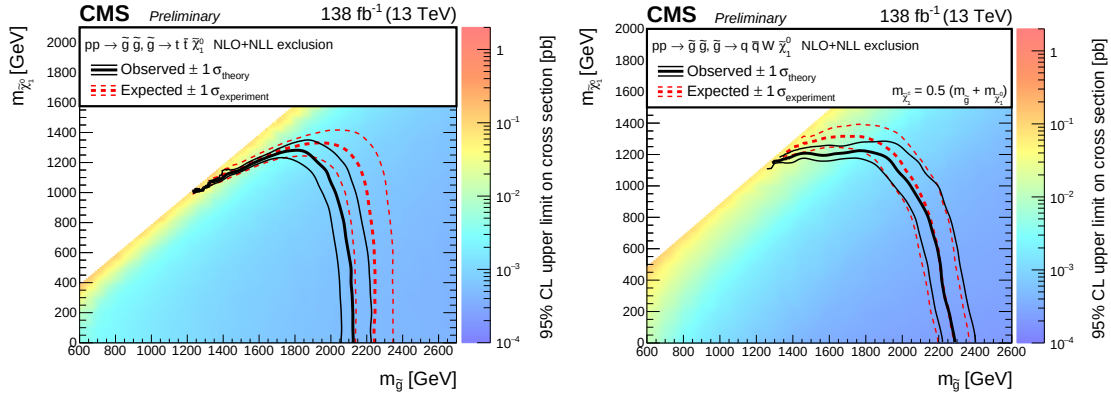

Figure 10: Cross section limits at 95% CL (left) for the T1tttt and (right) for the T5qqqqWW model, as a function of the gluino and LSP masses, assuming a branching ratio of 100%. The mass of the intermediate chargino is taken to be halfway between the gluino and the neutralino masses. The solid black (dashed red) lines correspond to the observed (expected) mass limits, with the thicker lines representing the central values and the thinner lines representing the $\pm 1\sigma$ uncertainty bands related to the theoretical (experimental) uncertainties.

10 Summary

A search for supersymmetry has been performed using a sample of proton-proton collisions at $\sqrt{s} = 13\,\text{TeV}$ with an integrated luminosity of $138\,\text{fb}^{-1}$, recorded by the CMS experiment. Events with a single charged lepton (electron or muon) and multiple jets are selected. Top quark and W boson tagging algorithms based on machine-learning techniques are employed to suppress the main background contributions in the analysis. Various exclusive search regions are defined that differ in the number of jets, the number of b-tagged jets, the number of hadronically decaying top quarks or W bosons, the scalar sum of all jet transverse momenta, and the scalar sum of the missing transverse momentum and the transverse momentum of the lepton.

To reduce the main background processes from $\text{t}\bar{\text{t}}$ and W+jets production, the presence of an electron or muon produced in the leptonic decay of a W boson in the event is exploited. Under the hypothesis that all of the missing transverse momentum in the event originates from the neutrino produced in a leptonic W boson decay, the W boson momentum is calculated. The requirement of a large azimuthal angle between the direction of the lepton and the reconstructed leptonic W boson notably reduces the background contributions.

The event yields observed in data are consistent with the expectations from the standard model processes, which are estimated using control samples in data and corrected for deviations observed in simulated event samples. Due to the absence of any significant excess of events, exclusion limits are evaluated on the supersymmetric particle masses in the context of two simplified models of gluino pair production.

For the T1tttt simplified model, where each gluino decays to a top quark-antiquark pair and the lightest neutralino, the excluded gluino masses reach up to 2130 GeV, while the excluded neutralino masses reach up to 1270 GeV. This result extends the exclusion limit on gluino (neutralino) masses from a previous CMS search [19] by about 320 (170) GeV.

The second simplified model, T5qqqqWW, also targets gluino pair production, but with decays to a light-flavor quark-antiquark pair and a chargino, which decays to a W boson and the lightest neutralino. The chargino mass in this decay channel is assumed to be $m_{\tilde{\chi}_1^\pm} = 0.5(m_{\tilde{g}} + m_{\tilde{\chi}_1^0})$. The excluded gluino masses reach up to 2280 GeV, while the excluded neutralino masses reach up to 1220 GeV. This corresponds to an improvement on gluino (neutralino) masses by about 380 (270) GeV in comparison with the previous result [19].

References

[1] J. Wess and B. Zumino, "A Lagrangian model invariant under supergauge transformations", *Phys. Lett. B* **49** (1974) 52, doi:10.1016/0370-2693(74)90578-4.

[2] P. Fayet and S. Ferrara, "Supersymmetry", *Phys. Rept.* **32** (1977) 249, doi:10.1016/0370-1573(77)90066-7.

[3] R. Barbieri, S. Ferrara, and C. A. Savoy, "Gauge models with spontaneously broken local supersymmetry", *Phys. Lett. B* **119** (1982) 343, doi:10.1016/0370-2693(82)90685-2.

[4] H. P. Nilles, "Supersymmetry, supergravity and particle physics", *Phys. Rept.* **110** (1984) 1, doi:10.1016/0370-1573(84)90008-5.

[5] H. E. Haber and G. L. Kane, "The search for supersymmetry: probing physics beyond the standard model", *Phys. Rept.* **117** (1985) 75, doi:10.1016/0370-1573(85)90051-1.

[6] S. P. Martin, "A supersymmetry primer", *Adv. Ser. Direct. High Energy Phys.* **21** (2010) 1, doi:10.1142/9789814307505_0001, arXiv:hep-ph/9709356.

[7] G. R. Farrar and P. Fayet, "Phenomenology of the production, decay, and detection of new hadronic states associated with supersymmetry", *Phys. Lett. B* **76** (1978) 575, doi:10.1016/0370-2693(78)90858-4.

[8] N. Arkani-Hamed et al., "MARMOSET: The path from LHC data to the new standard model via on-shell effective theories", 2007. arXiv:hep-ph/0703088.

[9] J. Alwall, P. Schuster, and N. Toro, "Simplified models for a first characterization of new physics at the LHC", *Phys. Rev. D* **79** (2009) 075020, doi:10.1103/PhysRevD.79.075020, arXiv:0810.3921.

[10] J. Alwall, M.-P. Le, M. Lisanti, and J. G. Wacker, "Model-independent jets plus missing energy searches", *Phys. Rev. D* **79** (2009) 015005, doi:10.1103/PhysRevD.79.015005, arXiv:0809.3264.

[11] D. Alves et al., "Simplified models for LHC new physics searches", *J. Phys. G* **39** (2012) 105005, doi:10.1088/0954-3899/39/10/105005, arXiv:1105.2838.

[12] CMS Collaboration, "Interpretation of searches for supersymmetry with simplified models", *Phys. Rev. D* **88** (2013) 052017, doi:10.1103/PhysRevD.88.052017, arXiv:1301.2175.

[13] ATLAS Collaboration, "Search for squarks and gluinos in final states with one isolated lepton, jets, and missing transverse momentum at $\sqrt{s} = 13$ TeV with the ATLAS detector", *Eur. Phys. J. C* **81** (2021) 600, doi:10.1140/s10052-021-09344-w, arXiv:2101.01629.

[14] ATLAS Collaboration, "Search for squarks and gluinos in events with an isolated lepton, jets, and missing transverse momentum at $\sqrt{s} = 13$ TeV with the ATLAS detector", *Phys. Rev. D* **96** (2017) 112010, doi:10.1103/PhysRevD.96.112010, arXiv:1708.08232.

[15] ATLAS Collaboration, "Search for supersymmetry in final states with missing transverse momentum and multiple b-jets in proton-proton collisions at $\sqrt{s} = 13$ TeV with the ATLAS detector", *JHEP* **06** (2018) 107, doi:10.1007/JHEP06(2018)107, arXiv:1711.01901.

[16] ATLAS Collaboration, "Search for gluinos in events with an isolated lepton, jets and missing transverse momentum at $\sqrt{s} = 13$ TeV with the ATLAS detector", *Eur. Phys. J. C* **76** (2016) 565, doi:10.1140/epjc/s10052-016-4397-x, arXiv:1605.04285.

[17] ATLAS Collaboration, "Search for pair production of gluinos decaying via stop and sbottom in events with b-jets and large missing transverse momentum in pp collisions at $\sqrt{s} = 13$ TeV with the ATLAS detector", *Phys. Rev. D* **94** (2016) 032003, doi:10.1103/PhysRevD.94.032003, arXiv:1605.09318.

[18] CMS Collaboration, "Search for supersymmetry in pp collisions at $\sqrt{s} = 13$ TeV with 137 fb^{-1} in final states with a single lepton using the sum of masses of large-radius jets", *Phys. Rev. D* **101** (2020) 052010, doi:10.1103/PhysRevD.101.052010, arXiv:1911.07558.

[19] CMS Collaboration, "Search for supersymmetry in events with one lepton and multiple jets exploiting the angular correlation between the lepton and the missing transverse momentum in proton-proton collisions at $\sqrt{s} = 13$ TeV", *Phys. Lett. B* **780** (2018) 384, doi:10.1016/j.physletb.2018.03.028, arXiv:1709.09814.

[20] CMS Collaboration, "Search for supersymmetry in events with one lepton and multiple jets in proton-proton collisions at $\sqrt{s} = 13$ TeV", *Phys. Rev. D* **95** (2017) 012011, doi:10.1103/PhysRevD.95.012011, arXiv:1609.09386.

[21] CMS Collaboration, "Search for supersymmetry in pp collisions at $\sqrt{s} = 13$ TeV in the single-lepton final state using the sum of masses of large-radius jets", *JHEP* **08** (2016) 122, doi:10.1007/JHEP08(2016)122, arXiv:1605.04608.

[22] CMS Collaboration, "Inclusive search for supersymmetry in pp collisions at $\sqrt{s} = 13$ TeV tev using razor variables and boosted object identification in zero and one lepton final states", *JHEP* **03** (2019) 031, doi:10.1007/JHEP03(2019)031, arXiv:1812.06302.

[23] CMS Collaboration, "Search for supersymmetry in pp collisions at $\sqrt{s} = 13$ TeV in the single-lepton final state using the sum of masses of large-radius jets", *Phys. Rev. Lett.* **119** (2017) 151802, doi:10.1103/PhysRevLett.119.151802, arXiv:1705.04673.

[24] ATLAS Collaboration, "Search for squarks and gluinos in final states with jets and missing transverse momentum using 139 fb^{-1} of $\sqrt{s} = 13$ TeV pp collision data with the ATLAS detector", *JHEP* **02** (2021) 143, doi:10.1007/JHEP02(2021)143, arXiv:2010.14293.

[25] ATLAS Collaboration, "Search for squarks and gluinos in final states with jets and missing transverse momentum using 36 fb^{-1} of $\sqrt{s} = 13$ TeV pp collision data with the ATLAS detector", *Phys. Rev. D* **97** (2018) 112001, doi:10.1103/PhysRevD.97.112001, arXiv:1712.02332.

[26] ATLAS Collaboration, "Summary of the searches for squarks and gluinos using $\sqrt{s} = 8$ TeV pp collisions with the ATLAS experiment at the LHC", *JHEP* **10** (2015) 054, doi:10.1007/JHEP10(2015)054, arXiv:1507.05525.

[27] ATLAS Collaboration, "Search for new phenomena in final states with large jet multiplicities and missing transverse momentum using $\sqrt{s} = 13$ TeV proton-proton collisions recorded by ATLAS in Run 2 of the LHC", *JHEP* **10** (2020) 062, doi:10.1007/JHEP10(2020)062, arXiv:2008.06032.

[28] CMS Collaboration, "Search for physics beyond the standard model in events with two leptons of same sign, missing transverse momentum, and jets in proton-proton collisions at $\sqrt{s} = 13$ TeV", *Eur. Phys. J. C* **77** (2017) 578, doi:10.1140/epjc/s10052-017-5079-z, arXiv:1704.07323.

[29] CMS Collaboration, "Search for new physics in events with same-sign dileptons and jets in pp collisions at $\sqrt{s} = 8$ TeV", *JHEP* **01** (2014) 163, doi:10.1007/JHEP01(2014)163, arXiv:1311.6736. [Erratum: doi:10.1007/JHEP01(2015)014].

[30] CMS Collaboration, "Search for supersymmetry in the multijet and missing transverse momentum final state in pp collisions at 13 TeV", *Phys. Lett. B* **758** (2016) 152, doi:10.1016/j.physletb.2016.05.002, arXiv:1602.06581.

[31] CMS Collaboration, "Search for supersymmetry in multijet events with missing transverse momentum in proton-proton collisions at 13 TeV", *Phys. Rev. D* **96** (2017) 032003, doi:10.1103/PhysRevD.96.032003, arXiv:1704.07781.

[32] CMS Collaboration, "Searches for physics beyond the standard model with the M_{T2} variable in hadronic final states with and without disappearing tracks in proton-proton collisions at $\sqrt{s} = 13$ TeV", *Eur. Phys. J. C* **80** (2020) 3, doi:10.1140/epjc/s10052-019-7493-x, arXiv:1909.03460.

[33] CMS Collaboration, "Search for supersymmetry in proton-proton collisions at 13 TeV in final states with jets and missing transverse momentum", *JHEP* **10** (2019) 244, doi:10.1007/JHEP10(2019)244, arXiv:1908.04722.

[34] CMS Collaboration, "Search for supersymmetry in proton-proton collisions at 13 TeV using identified top quarks", *Phys. Rev. D* **97** (2018) 012007, doi:10.1103/PhysRevD.97.012007, arXiv:1710.11188.

[35] CMS Collaboration, "Search for new phenomena with the M_{T2} variable in the all-hadronic final state produced in proton-proton collisions at $\sqrt{s} = 13$ TeV", *Eur. Phys. J. C* **77** (2017) 710, doi:10.1140/epjc/s10052-017-5267-x, arXiv:1705.04650.

[36] CMS Collaboration, "Performance of the CMS Level-1 trigger in proton-proton collisions at $\sqrt{s} = 13\,\text{TeV}$", *JINST* **15** (2020) P10017, doi:10.1088/1748-0221/15/10/P10017, arXiv:2006.10165.

[37] CMS Collaboration, "The CMS trigger system", *JINST* **12** (2017) P01020, doi:10.1088/1748-0221/12/01/P01020, arXiv:1609.02366.

[38] CMS Collaboration, "The CMS experiment at the CERN LHC", *JINST* **3** (2008) S08004, doi:10.1088/1748-0221/3/08/S08004.

[39] J. Alwall et al., "The automated computation of tree-level and next-to-leading order differential cross sections, and their matching to parton shower simulations", *JHEP* **07** (2014) 079, doi:10.1007/JHEP07(2014)079, arXiv:1405.0301.

[40] R. Frederix and S. Frixione, "Merging meets matching in MC@NLO", *JHEP* **12** (2012) 061, doi:10.1007/JHEP12(2012)061, arXiv:1209.6215.

[41] P. Nason, "A new method for combining NLO QCD with shower Monte Carlo algorithms", *JHEP* **11** (2004) 040, doi:10.1088/1126-6708/2004/11/040, arXiv:hep-ph/0409146.

[42] S. Frixione, P. Nason, and C. Oleari, "Matching NLO QCD computations with parton shower simulations: the POWHEG method", *JHEP* **11** (2007) 070, doi:10.1088/1126-6708/2007/11/070, arXiv:0709.2092.

[43] S. Alioli, P. Nason, C. Oleari, and E. Re, "A general framework for implementing NLO calculations in shower Monte Carlo programs: the POWHEG BOX", *JHEP* **06** (2010) 043, doi:10.1007/JHEP06(2010)043, arXiv:1002.2581.

[44] S. Alioli, P. Nason, C. Oleari, and E. Re, "NLO single-top production matched with shower in POWHEG: s- and t-channel contributions", *JHEP* **09** (2009) 111, doi:10.1088/1126-6708/2009/09/111, arXiv:0907.4076. [Erratum: doi:10.1007/JHEP02(2010)011].

[45] E. Re, "Single-top Wt-channel production matched with parton showers using the POWHEG method", *Eur. Phys. J. C* **71** (2011) 1547, doi:10.1140/epjc/s10052-011-1547-z, arXiv:1009.2450.

[46] T. Melia, P. Nason, R. Röntsch, and G. Zanderighi, "W^+W^-, WZ and ZZ production in the POWHEG BOX", *JHEP* **11** (2011) 078, doi:10.1007/JHEP11(2011)078, arXiv:1107.5051.

[47] P. Nason and G. Zanderighi, "W^+W^-, WZ and ZZ production in the POWHEG-BOX-V2", *Eur. Phys. J. C* **74** (2014) 2702, doi:10.1140/epjc/s10052-013-2702-5, arXiv:1311.1365.

[48] H. B. Hartanto, B. Jäger, L. Reina, and D. Wackeroth, "Higgs boson production in association with top quarks in the POWHEG BOX", *Phys. Rev. D* **91** (2015) 094003, doi:10.1103/PhysRevD.91.094003, arXiv:1501.04498.

[49] T. Sjöstrand et al., "An introduction to PYTHIA 8.2", *Comput. Phys. Commun.* **191** (2015) 159, doi:10.1016/j.cpc.2015.01.024, arXiv:1410.3012.

[50] S. Quackenbush, R. Gavin, Y. Li, and F. Petriello, "W physics at the LHC with FEWZ 2.1", *Comput. Phys. Commun.* **184** (2013) 209, doi:10.1016/j.cpc.2012.09.005, arXiv:1201.5896.

[51] R. Gavin, Y. Li, F. Petriello, and S. Quackenbush, "FEWZ 2.0: A code for hadronic Z production at next-to-next-to-leading order", *Comput. Phys. Commun.* **182** (2011) 2388, doi:10.1016/j.cpc.2011.06.008, arXiv:1011.3540.

[52] Y. Li and F. Petriello, "Combining QCD and electroweak corrections to dilepton production in the framework of the FEWZ simulation code", *Phys. Rev. D* **86** (2012) 094034, doi:10.1103/PhysRevD.86.094034, arXiv:1208.5967.

[53] T. Gehrmann et al., "W^+W^- production at hadron colliders in next to next to leading order QCD", *Phys. Rev. Lett.* **113** (2014) 212001, doi:10.1103/PhysRevLett.113.212001, arXiv:1408.5243.

[54] J. M. Campbell, R. K. Ellis, and C. Williams, "Vector boson pair production at the LHC", *JHEP* **07** (2011) 018, doi:10.1007/JHEP07(2011)018, arXiv:1105.0020.

[55] M. Beneke, P. Falgari, S. Klein, and C. Schwinn, "Hadronic top-quark pair production with NNLL threshold resummation", *Nucl. Phys. B* **855** (2012) 695, doi:10.1016/j.nuclphysb.2011.10.021, arXiv:1109.1536.

[56] M. Cacciari et al., "Top-pair production at hadron colliders with next-to-next-to-leading logarithmic soft-gluon resummation", *Phys. Lett. B* **710** (2012) 612, doi:10.1016/j.physletb.2012.03.013, arXiv:1111.5869.

[57] P. Bärnreuther, M. Czakon, and A. Mitov, "Percent-level-precision physics at the Tevatron: Next-to-next-to-leading order QCD corrections to $q\bar{q} \to t\bar{t} + X$", *Phys. Rev. Lett.* **109** (2012) 132001, doi:10.1103/PhysRevLett.109.132001, arXiv:1204.5201.

[58] M. Czakon and A. Mitov, "NNLO corrections to top-pair production at hadron colliders: the all-fermionic scattering channels", *JHEP* **12** (2012) 054, doi:10.1007/JHEP12(2012)054, arXiv:1207.0236.

[59] M. Czakon and A. Mitov, "NNLO corrections to top pair production at hadron colliders: the quark-gluon reaction", *JHEP* **01** (2013) 080, doi:10.1007/JHEP01(2013)080, arXiv:1210.6832.

[60] M. Czakon, P. Fiedler, and A. Mitov, "Total top-quark pair-production cross section at hadron colliders through $O(\alpha_S^4)$", *Phys. Rev. Lett.* **110** (2013) 252004, doi:10.1103/PhysRevLett.110.252004, arXiv:1303.6254.

[61] M. Czakon and A. Mitov, "TOP++: A program for the calculation of the top-pair cross-section at hadron colliders", *Comput. Phys. Commun.* **185** (2014) 2930, doi:10.1016/j.cpc.2014.06.021, arXiv:1112.5675.

[62] W. Beenakker et al., "NNLL-fast: predictions for coloured supersymmetric particle production at the LHC with threshold and Coulomb resummation", *JHEP* **12** (2016) 133, doi:10.1007/JHEP12(2016)133, arXiv:1607.07741.

[63] W. Beenakker, R. Höpker, M. Spira, and P. M. Zerwas, "Squark and gluino production at hadron colliders", *Nucl. Phys. B* **492** (1997) 51, doi:10.1016/S0550-3213(97)80027-2, arXiv:hep-ph/9610490.

[64] A. Kulesza and L. Motyka, "Threshold resummation for squark-antisquark and gluino-pair production at the LHC", *Phys. Rev. Lett.* **102** (2009) 111802, doi:10.1103/PhysRevLett.102.111802, arXiv:0807.2405.

[65] A. Kulesza and L. Motyka, "Soft gluon resummation for the production of gluino-gluino and squark-antisquark pairs at the LHC", *Phys. Rev. D* **80** (2009) 095004, doi:10.1103/PhysRevD.80.095004, arXiv:0905.4749.

[66] W. Beenakker et al., "Soft-gluon resummation for squark and gluino hadroproduction", *JHEP* **12** (2009) 041, doi:10.1088/1126-6708/2009/12/041, arXiv:0909.4418.

[67] W. Beenakker et al., "NNLL resummation for squark-antisquark pair production at the LHC", *JHEP* **01** (2012) 076, doi:10.1007/JHEP01(2012)076, arXiv:1110.2446.

[68] W. Beenakker et al., "Towards NNLL resummation: hard matching coefficients for squark and gluino hadroproduction", *JHEP* **10** (2013) 120, doi:10.1007/JHEP10(2013)120, arXiv:1304.6354.

[69] W. Beenakker et al., "NNLL resummation for squark and gluino production at the LHC", *JHEP* **12** (2014) 023, doi:10.1007/JHEP12(2014)023, arXiv:1404.3134.

[70] W. Beenakker et al., "Stop production at hadron colliders", *Nucl. Phys. B* **515** (1998) 3, doi:10.1016/S0550-3213(98)00014-5, arXiv:hep-ph/9710451.

[71] W. Beenakker et al., "Supersymmetric top and bottom squark production at hadron colliders", *JHEP* **08** (2010) 098, doi:10.1007/JHEP08(2010)098, arXiv:1006.4771.

[72] W. Beenakker et al., "NNLL resummation for stop pair-production at the LHC", *JHEP* **05** (2016) 153, doi:10.1007/JHEP05(2016)153, arXiv:1601.02954.

[73] M. L. Mangano, M. Moretti, F. Piccinini, and M. Treccani, "Matching matrix elements and shower evolution for top-pair production in hadronic collisions", *JHEP* **01** (2007) 013, doi:10.1088/1126-6708/2007/01/013, arXiv:hep-ph/0611129.

[74] CMS Collaboration, "Event generator tunes obtained from underlying event and multiparton scattering measurement", *Eur. Phys. J. C* **76** (2016) 155, doi:10.1140/epjc/s10052-016-3988-x, arXiv:1512.00815.

[75] CMS Collaboration, "Extraction and validation of a new set of CMS PYTHIA 8 tunes from underlying-event measurements", *Eur. Phys. J. C* **80** (2020) 4, doi:10.1140/epjc/s10052-019-7499-4, arXiv:1903.12179.

[76] NNPDF Collaboration, "Parton distributions with QED corrections", *Nucl. Phys. B* **877** (2013) 290, doi:10.1016/j.nuclphysb.2013.10.010, arXiv:1308.0598.

[77] NNPDF Collaboration, "Parton distributions from high-precision collider data", *Eur. Phys. J. C* **77** (2017) 663, doi:10.1140/epjc/s10052-017-5199-5, arXiv:1706.00428.

[78] GEANT4 Collaboration, "GEANT4—a simulation toolkit", *Nucl. Instrum. Meth. A* **506** (2003) 250, doi:10.1016/S0168-9002(03)01368-8.

[79] S. Abdullin et al., "The fast simulation of the CMS detector at LHC", in *Proceedings, 18th International Conference on Computing in High Energy and Nuclear Physics (CHEP 2010): Taipei, Taiwan, October 18-22, 2010*. 2011. [J. Phys. Conf. Ser. 331 (2011) 032049]. doi:10.1088/1742-6596/331/3/032049.

[80] A. Giammanco, "The fast simulation of the CMS experiment", in *Proceedings, 20th International Conference on Computing in High Energy and Nuclear Physics (CHEP 2013): Amsterdam, The Netherlands, October 14-18, 2013*. 2014. [J. Phys. Conf. Ser. 513 (2014) 022012]. doi:10.1088/1742-6596/513/2/022012.

[81] CMS Collaboration, "Particle-flow reconstruction and global event description with the CMS detector", *JINST* **12** (2017) P10003, doi:10.1088/1748-0221/12/10/P10003, arXiv:1706.04965.

[82] CMS Collaboration, "Technical proposal for the Phase-II upgrade of the Compact Muon Solenoid", CMS Technical Proposal CERN-LHCC-2015-010, CMS-TDR-15-02, 2015.

[83] CMS Collaboration, "Electron and photon reconstruction and identification with the CMS experiment at the CERN LHC", *JINST* **16** (2021) P05014, arXiv:2012.06888.

[84] CMS Collaboration, "Performance of the CMS muon detector and muon reconstruction with proton-proton collisions at $\sqrt{s} = 13\,\text{TeV}$", *JINST* **13** (2018) P06015, doi:10.1088/1748-0221/13/06/P06015, arXiv:1804.04528.

[85] M. Cacciari, G. P. Salam, and G. Soyez, "The anti-k_T jet clustering algorithm", *JHEP* **04** (2008) 063, doi:10.1088/1126-6708/2008/04/063, arXiv:0802.1189.

[86] M. Cacciari, G. P. Salam, and G. Soyez, "FastJet user manual", *Eur. Phys. J. C* **72** (2012) 1896, doi:10.1140/epjc/s10052-012-1896-2, arXiv:1111.6097.

[87] CMS Collaboration, "Pileup mitigation at CMS in 13 TeV data", *JINST* **15** (2020) P09018, arXiv:2003.00503.

[88] CMS Collaboration, "Jet energy scale and resolution in the CMS experiment in pp collisions at 8 TeV", *JINST* **12** (2017) P02014, doi:10.1088/1748-0221/12/02/P02014, arXiv:1607.03663.

[89] CMS Collaboration, "Identification of heavy-flavour jets with the CMS detector in pp collisions at 13 TeV", *JINST* **13** (2018) P05011, doi:10.1088/1748-0221/13/05/P05011, arXiv:1712.07158.

[90] CMS Collaboration, "Identification of heavy, energetic, hadronically decaying particles using machine-learning techniques", *JINST* **15** (2020) P06005, doi:10.1088/1748-0221/15/06/P06005, arXiv:2004.08262.

[91] CMS Collaboration, "Search for direct production of supersymmetric partners of the top quark in the all-jets final state in proton-proton collisions at $\sqrt{s} = 13\,\text{TeV}$", *JHEP* **10** (2017) 005, doi:10.1007/JHEP10(2017)005, arXiv:1707.03316.

[92] CMS Collaboration, "Performance of missing transverse momentum reconstruction in proton-proton collisions at $\sqrt{s} = 13\,\text{TeV}$ using the CMS detector", *JINST* **14** (2019) P07004, doi:10.1088/1748-0221/14/07/P07004, arXiv:1903.06078.

[93] C. G. Lester and D. J. Summers, "Measuring masses of semi-invisibly decaying particle pairs produced at hadron colliders", *Phys. Lett. B* **463** (1999) 99, doi:10.1016/S0370-2693(99)00945-4, arXiv:hep-ph/9906349.

[94] CMS Collaboration, "Measurement of the polarization of W bosons with large transverse momenta in W+jets events at the LHC", *Phys. Rev. Lett.* **107** (2011) 021802, doi:10.1103/PhysRevLett.107.021802, arXiv:1104.3829.

[95] CMS Collaboration, "Search for supersymmetry in pp collisions at $\sqrt{s} = 7$ TeV in events with a single lepton, jets, and missing transverse momentum", *Eur. Phys. J. C* **73** (2013) 2404, doi:10.1140/epjc/s10052-013-2404-z, arXiv:1212.6428.

[96] CMS Collaboration, "Precision luminosity measurement in proton-proton collisions at $\sqrt{s} = 13$ TeV in 2015 and 2016 at CMS", *Eur. Phys. J. C* **81** (2021) 800, doi:10.1140/epjc/s10052-021-09538-2, arXiv:2104.01927.

[97] CMS Collaboration, "CMS luminosity measurement for the 2017 data-taking period at $\sqrt{s} = 13$ TeV", CMS Physics Analysis Summary CMS-PAS-LUM-17-004, 2018.

[98] CMS Collaboration, "CMS luminosity measurement for the 2018 data-taking period at $\sqrt{s} = 13$ TeV", CMS Physics Analysis Summary CMS-PAS-LUM-18-002, 2019.

[99] Z. Bern et al., "Left-handed W bosons at the LHC", *Phys. Rev. D* **84** (2011) 034008, arXiv:1103.5445.

[100] CMS Collaboration, "Angular coefficients of Z bosons produced in pp collisions at $\sqrt{s} = 8$ TeV and decaying to $\mu^+\mu^-$ as a function of transverse momentum and rapidity", *Phys. Lett. B* **750** (2015) 154, doi:10.1016/j.physletb.2015.08.061, arXiv:1504.03512.

[101] ATLAS Collaboration, "Measurement of the polarisation of W bosons produced with large transverse momentum in pp collisions at $\sqrt{s} = 7$ TeV with the ATLAS experiment", *Eur. Phys. J. C* **72** (2012) 2001, doi:10.1140/epjc/s10052-012-2001-6, arXiv:1203.2165.

[102] G. Cowan, K. Cranmer, E. Gross, and O. Vitells, "Asymptotic formulae for likelihood-based tests of new physics", *Eur. Phys. J. C* **71** (2011) 1554, doi:10.1140/epjc/s10052-011-1554-0, arXiv:1007.1727. [Erratum: doi:10.1140/epjc/s10052-013-2501-z].

[103] T. Junk, "Confidence level computation for combining searches with small statistics", *Nucl. Instrum. Meth. A* **434** (1999) 435, doi:10.1016/S0168-9002(99)00498-2, arXiv:hep-ex/9902006.

[104] A. Read, "Presentation of search results: The CL_s technique", *J. Phys. G* **28** (2002) 2693, doi:10.1088/0954-3899/28/10/313.